Published in final edited form as:
*J Neurosci Res*. 2009 June ; 87(8): 1773–1793. doi:10.1002/jnr.22015.

# Spatiotemporal Ablation of Myelinating Glia-Specific *Neurofascin* (*Nfasc*$^{NF155}$) in Mice Reveals Gradual Loss of Paranodal Axoglial Junctions and Concomitant Disorganization of Axonal Domains

**Anilkumar M. Pillai**[1], **Courtney Thaxton**[1], **Alaine L. Pribisko**[1], **Jr-Gang Cheng**[2], **Jeffrey L. Dupree**[3], and **Manzoor A. Bhat**[1,2,4,5,*]

[1]Department of Cell and Molecular Physiology, University of North Carolina School of Medicine, Chapel Hill, North Carolina

[2]UNC-Neuroscience Center, University of North Carolina School of Medicine, Chapel Hill, North Carolina

[3]Department of Anatomy and Neurobiology, Virginia Commonwealth University, Richmond, Virginia

[4]Curriculum in Neurobiology, University of North Carolina School of Medicine, Chapel Hill, North Carolina

[5]Neurodevelopmental Disorders Research Center, University of North Carolina School of Medicine, Chapel Hill, North Carolina

## Abstract

The evolutionary demand for rapid nerve impulse conduction led to the process of myelination-dependent organization of axons into distinct molecular domains. These domains include the node of Ranvier flanked by highly specialized paranodal domains where myelin loops and axolemma orchestrate the axoglial septate junctions. These junctions are formed by interactions between a glial isoform of neurofascin (Nfasc$^{NF155}$) and axonal Caspr and Cont. Here we report the generation of myelinating glia-specific *Nfasc*$^{NF155}$ null mouse mutants. These mice exhibit severe ataxia, motor paresis, and death before the third postnatal week. In the absence of glial Nfasc$^{NF155}$, paranodal axoglial junctions fail to form, axonal domains fail to segregate, and myelinated axons undergo degeneration. Electrophysiological measurements of peripheral nerves from *Nfasc*$^{NF155}$ mutants revealed dramatic reductions in nerve conduction velocities. By using inducible PLP-CreER recombinase to ablate *Nfasc*$^{NF155}$ in adult myelinating glia, we demonstrate that paranodal axoglial junctions disorganize gradually as the levels of Nfasc$^{NF155}$ protein at the paranodes begin to drop. This coincides with the loss of the paranodal region and concomitant disorganization of the axonal domains. Our results provide the first direct evidence that the maintenance of axonal domains requires the fence function of the paranodal axoglial junctions. Together, our studies establish a central role for paranodal axoglial junctions in both the organization and the maintenance of axonal domains in myelinated axons.



*Correspondence to: Manzoor Bhat, Department of Cell and Molecular Physiology, University of North Carolina School of Medicine, Chapel Hill, NC 27599-7545. manzoor_bhat@med.unc.edu.

**Keywords**

myelin; myelinated axons; axonal domains; paranodes; axoglial junctions

The anatomical organization of myelinated axons into distinct molecular domains is the basis for rapid propagation of action potentials in a saltatory manner (Hartline and Colman, 2007). Although the signal transduction mechanisms that underlie the axonal organization into specific domains (i.e., the node, the paranode, the juxtaparanode, and the internode) are poorly understood, considerable progress has been made in identifying key molecular components within these axonal domains. The paranodal region is unique in its organization and ultrastructural characteristics and contains specialized axoglial junctions referred to as the *paranodal axoglial septate junctions*, which resemble the ladder-like invertebrate septate junctions (Einheber et al., 1997; Pedraza et al., 2001; Banerjee et al., 2006a, b). Three major paranodal proteins have been identified: Caspr or paranodin (Einheber et al., 1997; Menegoz et al., 1997; Peles et al., 1997; Bhat et al., 2001), and a GPI-anchored neural cell adhesion molecule Contactin (Cont; Berglund et al., 1999; Boyle et al., 2001) on the axonal side, and the 155-kDa neurofascin isoform ($Nfasc^{NF155}$) on the glial side (Tait et al., 2000; Charles et al., 2002). Although $Nfasc^{NF155}$ is the only known glial paranodal protein, many proteins expressed in myelinating glia are required at some level in the formation and/or stability of the paranodal junctions (Coetzee et al., 1996; Griffiths et al., 1998; Ishibashi et al., 2002; Lappe-Siefke et al., 2003; Southwood et al., 2004; Rasband et al., 2005).

Mutational analysis of *Caspr* and *Cont* loci revealed their essential roles in the formation of paranodal axoglial junctions and segregation of $Na^+$ and $K^+$ channels at the nodes and juxtaparanodes, respectively (Bhat et al., 2001; Boyle et al., 2001). Myelinated axons of *Caspr* mutants displayed disorganized paranodal regions with axonal cytoskeletal disorganization, resulting in organelle accumulation and axonal degeneration (Bhat et al., 2001; Einheber et al., 2006; Garcia-Fresco et al., 2006; Pillai et al., 2007 On the axonal cytoskeletal side, the cytoplasmic domain of Caspr assembles a protein complex that includes band 4.1B, αII and βII spectrins, and ankyrin B (Denisenko-Nehrbass et al., 2003; Garcia-Fresco et al., 2006; Ogawa et al., 2006). The localization of these proteins at the paranodes in *Caspr* mutants is disrupted, suggesting that Caspr is required for the formation of this paranodal cytoskeletal complex (Garcia-Fresco et al., 2006).

Recently, *Nfasc* mutants lacking both the glial $Nfasc^{NF155}$ and the neuronal $Nfasc^{NF186}$ isoforms were generated, and transgenic rescue of the glial and neuronal Nfasc isoforms indicated specific function of these isoforms in nodal organization (Sherman et al., 2005; Zonta et al., 2008). The *Nfasc* mutants died at about postnatal day (P) 6, when paranodal and nodal organization has not been completed and myelination is still taking place. This early lethality combined with the loss of both $Nfasc^{NF155}$ and $Nfasc^{NF186}$ isoforms has hampered a detailed phenotypic analysis to determine the specific role of glial $Nfasc^{NF155}$ in the formation and function of the axoglial junctions. In this study, using embryonic and adult gene disruption strategies, we have specifically addressed the role of myelinating glia-specific $Nfasc^{NF155}$ in the formation and maintenance of the paranodal axoglial junctions, without affecting the function of neuronal $Nfasc^{NF186}$. We show that embryonic loss of glial $Nfasc^{NF155}$ in mice results in motor coordination defects, loss of paranodal axoglial junctions, a significant delay in nerve conduction velocity, and lethality at P17. We further demonstrate that ablation of $Nfasc^{NF155}$ in adult myelinating glia results in a gradual loss of paranodal axoglial junctions and a concomitant disorganization of the axonal domains. Together our results establish that paranodal axoglial junctions are central to domain organization and maintenance in myelinated axons.

# MATERIALS AND METHODS

## Animals

All animal experiments were carried out according to UNC-IACUC-approved guidelines for ethical treatment of laboratory animals. Transgenic mice used in this study expressing *Cre* recombinase from the *Cnp* locus (*Cnp-Cre*; Lappe-Siefke et al., 2003), the *P0* promoter (Feltri et al., 1999), and inducible *Plp-CreER* (Doerflinger et al., 2003) were generously provided by Drs. Klaus Nave (Max Planck Institute of Experimental Medicine), Laura Feltri (San Rafaele Scientific Institute, Italy), and Brian Popko (University of Chicago), respectively.

## Conditional Targeting of *Nfasc* Gene

The *neurofascin* (*Nfasc*) gene spans ~171 kb of the genomic DNA and generates many alternative spliced mRNAs (refer http://www.ensemble.org/mouse). To ablate *Nfasc* gene expression and function conditionally, a targeting construct was generated in which *loxP* sites were targeted to flank exons 2 and 3 of the *Nfasc* gene. A BAC clone (*bMQ228D3*) from a *129 AB2.2* BAC library containing the targeted *Nfasc* exons was obtained from the Sanger Center, England. With BAC recombineering technology, a polymerase II promoter directed diphtheria toxin (DT) vector containing short PCR-generated arms homologous to those of the *Nfasc* DNA sequence was transformed into *Escherichia coli DY380* recombinant bacterial strain (heat-induced *RED* and *GAM* recombinase complex) containing the *Nfasc* BAC. By this approach, an ~9.4-kb fragment from *Nfasc* BAC was successfully retrieved into the DT vector by means of gap repair. The first *loxP* site was inserted into intron 3 by transforming a *PGK-neo* cassette flanked with *loxP* sites. This confers kanamycin resistance to *DT-Nfasc* plasmid. The *DT-Nfasc* clone with proper *neo cassette* integration was transformed into strain *EL350*, and, upon arabinose-induced Cre recombination in transformed *EL350*, the *neo* cassette was removed, leaving the *loxP* site in intron 3. Similar steps were repeated for the insertion of another *neo* cassette flanked with *FRT* and *FRT-loxP* sites into intron 1. Prior to ES cell targeting, the functionality of the *loxP* sites as well as the expected restriction enzyme digestion patterns in the targeting vector was confirmed. The targeting construct was linearized with NotI, followed by electroporation into ES cells. The targeted ES cells were screened by PCR amplification and standard molecular biological methods (for details see Bhat et al., 2001).

## Antibodies, Immunofluorescence, and Immunoblotting

Three antisera were generated against the two Nfasc protein isoforms as follows. Sequences corresponding to the $Nfasc^{NF155}$-specific fibronectin III domain 3 (amino acids KIRV--ASFP), the $Nfasc^{NF186}$-specific mucin domain (amino acids TVGT--VYSR), and the common cytoplasmic region (amino acids FIKR--YSLA) were used to immunize guinea pigs and rats as previously described (Bhat et al., 1999, 2001). Other primary antibodies used were guinea pig anti-Caspr antibodies (Bhat et al., 2001), rabbit anticalbindin, mouse pansodium channel, rabbit and mouse antipotassium channel ($K_v1.1$; Sigma, St. Louis, MO), mouse anti-β-tubulin (Chemicon, Temecula, CA), mouse anti-PLP (ABR Bioreagents), mouse anti-MBP (Sterberger Monoclonals, Lutherville, MD), rabbit anti-NrCAM (Abcam, Cambridge, MA), rat anti-PLP (A. Gow, Wayne State University), and rabbit anti-Cont (J. Salzer, NYU; Rios et al., 2000). The secondary antibodies conjugated to Alexa Fluors-488, -568 and -647 were obtained from Invitrogen Corporation (La Jolla, CA).

## Preparation of Teased Sciatic Nerves and Cerebellar and Spinal Cord Sections

Fixed sciatic nerves were teased into individual fibers in ice-cold PBS, mounted on glass slides, and dried overnight at RT, followed by treatment with acetone at −20°C for 20 min. The slides were washed with PBS several times before immunostaining; in some cases, slides were stored at −80°C until processed further. For cerebellar and spinal cord sections, wild-type and mutant

mice were deeply anesthetized and transcardially perfused with saline buffer followed by a solution of 4% paraformaldehyde in PBS. For immunofluorescence, cerebelli or spinal cords were sectioned on a Vibratome (Leica) at 30 μm thickness and processed as previously described (Garcia-Fresco et al., 2006).

## Transmission Electron Microscopy

TEM was carried out essentially as described by Garcia-Fresco et al. (2006). After intracardiac perfusion, the whole animal was postfixed for 2 weeks at 4°C in the same fixation solution. After an overnight incubation in Millonig's buffer, nerve fibers, spinal cords, or cerebellar tissue from each animal was postfixed for 1 hr in cacodylate-buffered 1% osmium tetroxide. The tissue was then rinsed, dehydrated in increasing concentrations of cold ethanol, and infiltrated and embedded in PolyBed (Polysciences, Warrington, PA). One-micrometer and ninety-nanometer sections were cut and stained with to-luidine blue or a combination of uranyl acetate and lead citrate, respectively. The 1-μm-thick sections were analyzed with a Nikon Eclipse 800, and the 90-nm-thick sections were analyzed with a JEOL JEM1230 transmission electron microscope equipped with a Gatan Ultrascan digital camera for acquiring images at high resolution.

## Image Analysis and Quantitation

Confocal images were captured with a Bio-Rad Radiance 2000 laser scanning system attached to a Zeiss Axioplan2 microscope. The immunofluorescence images shown are Z stacks of five to eight sections with a scan step of 0.25 μm. All scanning parameters were optimized for the wild-type tissues, and the mutant tissues were scanned at identical settings. Quantitative measurements were performed on at least three independent tissue samples for immunofluorescence analysis and two independent samples for TEM analysis. For paranodal numbers and length estimation, only those paranodes were counted that looked morphologically normal and did not display structural distortions or stretching as a result of teasing of the fibers during preparation.

## Tamoxifen-Induced Nuclear Translocation of CreER Recombination

The tamoxifen induction experiments were carried out essentially according to Doerflinger et al. (2003). Animals of the genotype *Plp-CreER;Nfasc*$^{Flox}$/+ and *Plp-CreER;Nfasc*$^{Flox}$ were intraperitoneally injected with 100 μl of suspension (=1 mg tamoxifen) for 10 consecutive days beginning at P23. The animals were then sacrificed at various time points for phenotypic analysis by light and electron microscopy and for electrophysiological measurements.

## Electrophysiological Studies

Age-matched wild-type, *Cnp-Cre;Nfasc*$^{Flox/Flox}$, *P0- Cre;Nfasc*$^{Flox/Flox}$, and *Plp-CreER;Nfasc*$^{Flox/Flox}$ mutant mice were deeply anesthetized with Avertin or sacrificed by cervical dislocation. Left tibial/plantar nerves (mean length 13.5 mm) were carefully dissected free, cleaned of excess connective tissue, and maintained in cooled, oxygenated, modified Bretag's solution (123 mM NaCl, 3.5 mM KCl, 0.7 mM $MgSO_4$, 2 mM $CaCl_2$, 9.5 mM Na gluconate, 1.7 mM $NaH_2PO_4$, 5.5 mM glucose, 7.5 mM sucrose, 10 mM HEPES; pH 7.40, osmolarity 290) for 2 hr to permit recovery from the acute injury of the dissection. In a dual-compartment ex vivo recording chamber (Stampfli, 1954; Reeh, 1986), the nerves were superfused in oxygenated Bretag's solution at 30°C. Rectangular wave pulses (0.01 msec) were delivered by an Ag/AgCl suction electrode to the proximal portion of the nerve. One millimeter of the distal portion of the nerve was pulled out of the solution, suspended in a layer of mineral oil, and positioned on a gold recording electrode. A reference electrode was placed in solution close to the gold recording electrode. Evoked compound action potentials (CAP) were amplified and stored as digitized signals with pClamp 10.2 software (Molecular Devices, Union

City, CA). Amplitude of the stimulus pulses (10–30 V) was adjusted to ensure a near-maximal stimulation of the A-component of the CAP (Gasser and Grundfest, 1939). In other words, the nerve was stimulated at an intensity sufficient to elicit a stable A-component amplitude and latency. Conduction latency was measured as the time in milliseconds from the start of the stimulus artifact to the start of the first upward deflection of the A-component. Conduction velocity (m/sec) was calculated as the distance between the stimulating and recording electrodes divided by the conduction latency.

## RESULTS

### Generation and Phenotypic Characterization of Myelinating Glia-Specific *Neurofascin* (*Nfasc*$^{NF155}$) Null Mutants

The main molecular components of the paranodal axoglial junctional complex include Caspr and its cis interacting partner Cont on the axonal side and the Nfasc$^{NF155}$ on the glial side (Fig. 1A; Peles and Salzer, 2000;Pedraza et al., 2001;Bhat, 2003;Salzer, 2003). Recently, *Nfasc* mutants were generated revealing that *Nfasc* is required for the formation of paranodal axoglial junctions and organization of the node of Ranvier (Sherman et al., 2005). We first determined the molecular differences between the glial and the neuronal isoforms of *Nfasc* by analyzing the reported *Nfasc* cDNA sequences and the mouse genomic DNA databases (for details see http://www.ensembl.org/mouse). This analysis revealed that the major *Nfasc* isoforms contain 28 exons, with *Nfasc*$^{NF155}$ containing exons 20 and 21, encoding the third fibronectin (FN) III domain (Fig. 1B, exons in gray). *Nfasc*$^{NF186}$ instead contains exons 23 and 24, which are absent in *Nfasc*$^{NF155}$, encoding the mucin (MUC) domain (Fig. 1B, exons in dark gold; Davis et al., 1996;Tait et al., 2000).

To ablate the function of *Nfasc*$^{NF155}$ specifically without interfering with the function of *Nfasc*$^{NF186}$, we first analyzed the structure of the 5′ region of the *Nfasc* locus. We generated a targeting construct (*Nfasc*$^{Flox}$) such that the coding exons 2 and 3 were flanked by *loxP* sites. Myelinating glia-specific Cre-mediated recombination resulted in the deletion of exons 2/3, causing translation termination of *Nfasc*$^{NF155}$ in exon 4 (Fig. 1C). A 30-amino-acid polypeptide from the putative initiation codon and 20 unrelated amino acids were produced as a result of frame shift without affecting neuronal *Nfasc*$^{NF186}$ expression (Fig. 1C, red asterisk). A detailed strategy for the generation of the *Nfasc*$^{Flox}$ targeting construct is given in Materials and Methods. After germline transmission, heterozygous and homozygous mice were confirmed by PCR amplification across the targeted region. The primer combinations and the products of the PCR amplification from wild-type (+/+), *Nfasc*$^{Flox/+}$, *Nfasc*$^{Flox/Flox}$, and Cnp-Cre-mediated deletion of the floxed exons are shown in Figure 1D. The PCR amplification using primer sets 1 and 4 confirmed that both exons 2 and 3 were deleted in *Cnp-cre/+;Nfasc*$^{Flox/Flox}$ (Fig. 1D).

To ablate the expression of *Nfasc*$^{NF155}$ specifically in the myelinating glial cells in the CNS and PNS, we used two well-established myelinating glia-specific Cre lines, *Cnp-cre* (Lappe-Siefke et al., 2003) and myelin *P0-cre* (Feltri et al., 1999). The mice of the genotype *Cnpcre/+;Nfasc*$^{Flox/Flox}$, in which only *Nfasc*$^{NF155}$ has been ablated in both the Schwann cells and the oligodendrocytes, are born at the expected Mendelian frequency from heterozygous intercrosses. The *Nfasc*$^{NF155}$ mutant mice are indistinguishable from their wild-type littermates until approximately P8. Starting at about P12, the mice become identifiable by their smaller stature and progressive neurological defects that reach maximal severity toward the beginning of the third postnatal week, and all mutants die at about P16/17. A typical P16 *Cnpcre/+;Nfasc*$^{Flox/Flox}$ animal has a posture shown in Figure 1F and is easily differentiated from the wild type shown in Figure 1E. At P16, the defects include hypomotility and severe motor coordination defects. These mice fail to maintain their balance on a stationary beam and are nearly immobile in open field tests (data not shown). We monitored the weight of the *Cnp-cre/*

*+;Nfasc*$^{Flox/Flox}$ animals and compared it with that of their wild-type littermates. As shown in Figure 1G, at about P6, the wild-type and *Cnp-cre/+;Nfasc*$^{Flox/Flox}$ littermates are of almost identical weight, but, from P8 onward, the *Cnp-cre/+;Nfasc*$^{Flox/Flox}$ animals begin to show progressive loss of weight, and, by P16/17, the weight of the *Cnp-cre/+;Nfasc*$^{Flox/Flox}$ animals falls below what they had weighed at P6. The *Cnp-cre/+;Nfasc*$^{Flox}$/+ are indistinguishable from their wild-type littermates and live a normal life span without displaying any physical or behavioral phenotypes. In contrast to *Nfasc* mutants reported by Sherman et al. (2005), which die at P6 when paranodal and nodal organization is just taking place, our *Cnpcre/+;Nfasc*$^{Flox/Flox}$ mice die at P16/17, emphasizing the role of individual Nfasc isoforms in paranodal and nodal organization.

To demonstrate that we had specifically generated an *Nfasc*$^{NF155}$ null allele in myelinating glia, we carried out Western blot analysis using antisera generated against the C-terminal domain of Nfasc (NFCT), which recognizes both Nfasc$^{NF155}$ and Nfasc$^{NF186}$. As shown in Figure 1H, the wild-type (+/+) spinal cord lysate shows both Nfasc$^{NF155}$ and Nfasc$^{NF186}$ protein isoforms (arrows), whereas *Cnp-cre/+;Nfasc*$^{Flox/Flox}$ animals show only the *Nfasc*$^{NF186}$ isoform and lacks the *Nfasc*$^{NF155}$ isoform (red asterisk). These results indicate specific loss of *Nfasc*$^{NF155}$ in the myelinating glial cells. To establish that the *Nfasc*$^{NF155}$ isoform is absent from the paranodes of the myelinated axons, we immunostained teased sciatic nerve fibers with isoform-specific antibodies against *Nfasc*$^{NF155}$ and *Nfasc*$^{NF186}$ (Fig. 1B). As shown in Figure 1I,J and in the merged image in Figure 1I″, wildtype (+/+) fibers showed specific paranodal localization of Nfasc$^{NF155}$ (Fig. 1I, green), and nodal localization of Nfasc$^{NF186}$ (Fig. 1I′, red). The *Cnp-cre/+;Nfasc*$^{Flox/Flox}$ mutant sciatic nerve fibers lacked immunoreactivity against Nfasc$^{NF155}$ (Fig. 1J, green) but showed normal nodal localization of Nfasc$^{NF186}$ (Fig. 1J′, red) in the merged image (Fig. 1J″). Similarly *P0-cre/+;Nfasc*$^{Flox/Flox}$ mice revealed loss of Nfasc$^{NF155}$ specifically in the peripheral nerve fibers both by immunoblot and by immunohistochemical analyses and not in the central myelinated fibers (data not shown). Taken together, our data demonstrate that we have generated myelinating gliaspecific *Nfasc*$^{NF155}$ mutants without altering the expression and localization of *Nfasc*$^{NF186}$ at the node of Ranvier.

## Axonal Domain Organization is Disrupted in *Nfasc*$^{NF155}$ Mutant Myelinated Axons

To determine the relationship between expression of the Nfasc isoforms with paranodal biogenesis, we first analyzed the developmental expression profile of Nfasc$^{NF155}$ in myelinated sciatic nerve fibers by using immunohistochemistry. As shown in Figure 2A, at P0, Nfasc$^{NF155}$ is expressed at the sites where paranodes are beginning to form. At this stage, Nfasc$^{NF186}$ localizes to the node, which shows a broad morphology (Fig. 2Aa, red). Similarly, we analyzed P1, P3, P5, P10, and P15 sciatic nerves, which revealed that Nfasc$^{NF155}$ is expressed at the paranodes during their formation. At P10 and P15, as paranode formation is completed, Nfasc$^{NF186}$ localization becomes more concentrated at the node (compare Fig. 2Aa–f). We next analyzed the distribution of Nfasc$^{NF155}$ along with the axonal paranodal protein Caspr and nodal Nfasc$^{NF186}$ to determine their precise colocalization during paranode formation. As shown in Figure 2B, Nfasc$^{NF155}$ (green) colocalizes with Caspr at the paranodes (blue) at all postnatal developmental stages beginning with P0 through P15. The immunoreactivity for Caspr at P0 is qualitatively lower compared with later stages. From P3 onward, Nfasc$^{NF155}$ and Caspr showed complete colocalization (Fig. 2Bc–f). To establish the comparative expression levels of Nfasc$^{NF155}$ and Nfasc$^{NF186}$ during postnatal development, we carried out Western blot analysis of P1, P3, P6, P8, P12, and P15 spinal cords using NFCT antibodies that recognize both isoforms. As shown in Figure 2C, Nfasc$^{NF186}$ protein levels are comparatively higher than Nfasc$^{NF155}$ at early stages (Fig. 2C, compare P1 and P3). At later stages, Nfasc$^{NF155}$ expression levels increase compared with earlier stages and with Nfasc$^{NF186}$ (Schafer et al., 2006). These results are consistent with the increase in

Nfasc$^{NF155}$ fluorescence observed at later developmental stages in the immunohistochemical analysis shown in Figure 2A,B. Thus Nfasc$^{NF155}$ expression pattern coincides with paranode formation during postnatal development.

To establish the consequence of loss of Nfasc$^{NF155}$ in the Schwann cells in *Cnp-cre/+;Nfasc$^{Flox/Flox}$* animals, we analyzed mutant sciatic nerve fibers by coimmunostaining against Caspr and Cont paranodal proteins along with nodal Nfasc$^{NF186}$. Wild-type nerve fibers from P17 animals show the expected localization of Nfasc$^{NF155}$ at the paranodes (Fig. 2D, red), and Nfasc$^{NF186}$ localization at the node (Fig. 2D′, green, see also merged image in Fig. 2D″). Similarly, immunostaining with NFCT antibodies reveals proper paranodal localization of Nfasc$^{NF155}$ (Fig. 2E–E″). In *Cnp-cre/+;Nfasc$^{Flox/Flox}$* animals, NFCT immunoreactivity indicates specific loss of *Nfasc$^{NF155}$* at the paranodes without affecting *Nfasc$^{NF186}$* (Fig. 2F, red), as is seen with Nfasc$^{NF186}$ specific immunoreactivity (Fig. 2F′, green; also shown in the merged image in Fig. 2F″,F‴). Immunostaining against Caspr in the wild-type (Fig. 2G, red) and *Cnp-cre/+;Nfasc$^{Flox/Flox}$* animals (Fig. 2H, red) and against Cont in the wild-type (Fig. 2I, red) and *Cnp-cre/+;Nfasc$^{Flox/Flox}$* animals (Fig. 2J, red) shows that both Caspr and Cont fail to localize at the paranodes in the *Cnp-cre/+;Nfasc$^{Flox/Flox}$* animals. These results indicate that glial Nfasc$^{NF155}$ is essential for paranodal Caspr and Cont localization and that the localization of nodal Nfasc$^{NF186}$ is not affected in *Cnp-cre/+;Nfasc$^{Flox/Flox}$* mutant fibers.

A hallmark of myelinated axons is the localization of voltage-gated $Na^+$ channels at the nodes and the delayed rectifier Shaker-type $K^+$ channels at the juxtaparanodes and to regions of the internode that oppose the noncompacted myelin membranes, e.g., the Schmidt-Lanterman incisures and the internal mesaxon (Arroyo et al., 1999). To determine whether loss of Nfasc$^{NF155}$ at the paranodal junctions in *Cnp-cre/+;Nfasc$^{Flox/Flox}$* mice affects the distribution of these channels, we carried out immunofluorescence staining of sciatic nerves. In both wild-type (Fig. 2K) and *Cnp-cre/+;Nfasc$^{Flox/Flox}$* (Fig. 2L) mice, $Na^+$ channels (Fig. 2K,L, green) were restricted to the nodes of Ranvier. Unlike the localization of $Na^+$ channels, the distribution of the $K^+$ channels (Fig. 2K,L, $K_v$1.1, red) was markedly different between the wild-type and the *Cnp-cre/+;Nfasc$^{Flox/Flox}$* mice. In wild-type nerves (Fig. 2K), $K^+$ channels were completely separated from the $Na^+$ channels by the paranodal region, as expected. In contrast, *Cnp-cre/+;Nfasc$^{Flox/Flox}$* mice showed mislocalized $K^+$ channels in the paranodal region, immediately adjacent to and, in some cases, slightly overlapping with $Na^+$ channels (note the areas of overlap appear as yellow in the merged images; Fig. 2L). These data indicate that glial Nfasc$^{NF155}$ at the paranodal axoglial junctions is required for the segregation of $Na^+$ and $K^+$ channels into distinct domains.

To characterize further the role of Nfasc$^{NF155}$ in myelinated axons, we coimmunostained sciatic nerve fibers from wild-type (Fig. 2M,N) and *Cnp-cre/+;Nfasc$^{Flox/Flox}$* (Fig. 2O) mice and analyzed them at low magnification. As shown in Figure 2M, an entire internodal segment flanked with two nodes was immunostained against $Na^+$ channels (green arrows), and paranodes were immunostained against Caspr (blue) and $K^+$ channels ($K_v$1.1, red) with distinct localization at the juxtaparanodal region and Schmidt-Lanterman incisures (red arrows) and inner mesaxon spanning the internodal region. Immunostaining of the wild-type sciatic nerves with antibodies against NFCT (Fig. 2N, green), $Na^+$ channels (Fig. 2N, blue), and $K^+$ channels (Fig. 2N, $K_v$1.1, red) revealed that Nfasc$^{NF155}$ is strongly expressed in the internodal region at Schmidt-Lanterman incisures (green arrows). The Nfasc$^{NF155}$ immunoreactivity either overlaps or is present adjacent to $K^+$ channel immunoreactivity (Fig. 2N, red and green arrows). Immunostaining of sciatic nerve fibers from *Cnp-cre/+;Nfasc$^{Flox/Flox}$* mice revealed that *Nfasc$^{NF155}$* immunoreactivity along the internodes at the Schmidt-Lanterman incisures is absent (Fig. 2O, green) and that the localization of $K^+$ channels at or near the incisures is compromised (Fig. 2O, red). These data suggest that Nfasc$^{NF155}$ expressed by myelinating Schwann cells may be required for the formation of internodal specializations.

To establish that loss of Nfasc$^{NF155}$ also affected central myelinated axons, we carried out immunofluorescence analysis of the spinal cords from wild-type and *Cnp-cre/+;Nfasc$^{Flox/Flox}$* mice. As shown in Figure 2P, wild-type spinal cord white matter immunostained against NFCT (blue) and NF186 (red) showed paranodal Nfasc$^{NF155}$ (blue) and nodal Nfasc$^{NF186}$ localization (pink, because both antibodies recognize Nfasc$^{NF186}$). The spinal cord white matter from *Cnp-cre/+;Nfasc$^{Flox/Flox}$* mice, immunostained with the same antibodies as in Figure 2P, showed no immunoreactivity against Nfasc$^{NF155}$ but showed normal localization of Nfasc$^{NF186}$ (Fig. 2Q, pink), indicating specific loss of Nfasc$^{NF155}$ in the oligodendrocytes. We also analyzed the domain organization in the spinal cord white matter by using coimmunostaining against Caspr (Fig. 2R,S, blue), NF186 (green) and $K_v$1.1 (red). As observed in the PNS, the spinal cord also revealed loss of the paranodal domain and absence of segregation between the juxtaparanodal and the nodal components (Fig. 2S).

To determine further whether loss of glial Nfasc$^{NF155}$ phenocopied the presence of axonal swellings in the cerebellar Purkinje neurons, as was observed in *Caspr* (Garcia-Fresco et al., 2006; Pillai et al., 2007), *Cont* (Boyle et al., 2001), and CGT (Garcia-Fresco et al., 2006) mutants, we carried out immunostaining of the cerebella from wild-type and *Cnp-cre/+;Nfasc$^{Flox/Flox}$* mice with anticalbindin antibodies. As shown in Figure 2T,U, wild-type Purkinje neuron axons displayed normal axonal morphology. In contrast, Purkinje axons from *Cnp-cre/+;Nfasc$^{Flox/Flox}$* mice displayed extensive presence of axonal swellings (Fig. 2V,W). These swellings are reminiscent of those observed in *Caspr* and *CGT* mutants, which we had previously shown to be caused by cytoskeletal abnormalities and accumulation of the cellular organelles at the disrupted paranodal regions (Garcia-Fresco et al., 2006). To establish further that loss of glial Nfasc$^{NF155}$ did not alter the protein expression levels of myelin or paranodal proteins, we carried out Western blot analysis of brain lysates from wild-type and *Cnp-cre/+;Nfasc$^{Flox/Flox}$* mice. As shown in Figure 2X, the protein levels of the paranodal proteins Caspr and Cont and the myelin proteins proteolipid protein (PLP) and myelin basic protein (MBP) between the wild-type and *Cnp-cre/+;Nfasc$^{Flox/Flox}$* mice revealed no significant differences. These results indicate that loss of glial Nfasc$^{NF155}$ does not alter the steady-state levels of paranodal or myelin proteins. Taken together, our data demonstrate that loss of glial Nfasc$^{NF155}$ results in the disruption of the paranodal region and failure to segregate the axonal domains in the myelinated axons.

## *Nfasc$^{NF155}$* Mutants Fail To Establish Paranodal Axoglial Junctions

As established above, myelinating glia-specific loss of Nfasc$^{NF155}$ did not alter myelin protein levels; therefore, we wanted to determine whether histological organization of the nervous system, including myelination, was affected. Light microscopy did not reveal any obvious abnormalities in the histological organization or the extent of myelination (data not shown). As shown in Figure 3, the myelinated sciatic nerve fibers from the wild-type (Fig. 3A) and *Cnp-cre/+;Nfasc$^{Flox/Flox}$* (Fig. 3B) mice were indistinguishable, and morphometric analysis of the myelinated fibers in the PNS showed no significant differences in axon and nerve fiber diameters, myelin thickness, or the g value (ratio of axon to fiber diameter; data not shown). These results, together with the normal myelin protein levels (Fig. 2X), suggest that lack of Nfasc$^{NF155}$ does not result in any significant alterations in the myelination process.

Because immunofluorescence analysis established that Nfasc$^{NF155}$ was localized to the myelin side of the paranodal region, and loss of Nfasc$^{NF155}$ specifically in myelinating glia resulted in mislocalization of Caspr and Cont, we examined the ultrastructure of the paranodal region in the PNS and CNS. As shown in Figure 3, low-magnification images of the sciatic nerve nodal and paranodal regions from wild-type (Fig. 3C) and *Cnp-cre/+;Nfasc$^{Flox/Flox}$* (Fig. 3D) mice reveal no major anatomical or organizational abnormalities. At higher magnification, the paranodal region in the wild-type showed myelin loops arrayed sequentially and in close

apposition to the axonal membrane (Fig. 3E). Between the loops and the axon, periodic densities corresponding to the septate-like transverse bands were readily apparent (Fig. 3E, black arrowheads). In the *Cnp-cre/+;Nfasc*$^{Flox/Flox}$ sciatic nerve fibers, the organization of the paranodal loops was preserved; however, the characteristic transverse bands were consistently absent (Fig. 3F,G, black arrowheads). In addition, the spacing between the paranodal loops and the axolemma was often abnormally wide, and the normal indentation of the axolemma by the paranodal loops was often absent (compare Fig. 3F–H with E). A consistent abnormality observed was the absence of the regular array of transverse bands between the paranodal loops and the axon. This was further confirmed by analyzing the Schwann cell-specific *P0-cre/+; Nfasc*$^{Flox/Flox}$ sciatic nerve fibers (Fig. 3I). Interestingly, the *P0-cre/+; Nfasc*$^{Flox/Flox}$ mice do not show any significant peripheral neurological deficits until P90. However, it remains to be seen whether older *P0-cre/+;Nfasc*$^{Flox/Flox}$ mice will develop any severe peripheral nerve functional abnormalities. Furthermore, the *Cnp-cre/+;Nfasc*$^{Flox/Flox}$ sciatic nerve fibers showed accumulation of organelles, such as mitochondria, and nodal membrane folds resulting from cytoskeletal abnormalities at the nodal/paranodal region (Fig. 3G). Together these data reveal that loss of Nfasc$^{NF155}$ in Schwann cells results in the loss of paranodal axoglial septate junctions.

Aside from the Nfasc$^{NF155}$ localization to paranodes in the PNS, it also localizes to CNS paranodal junctions; therefore, we examined the ultrastructure of this region in the spinal cord and cerebella of *Cnp-cre/+;Nfasc*$^{Flox/Flox}$ mice. As shown in Figure 4A, in the wild-type spinal cord white matter, the paranodal loops are arrayed in close apposition to the axonal membrane, which establishes the septate-like transverse bands (black arrowheads). In contrast, the paranodal loops in *Cnp-cre/+;Nfasc*$^{Flox/Flox}$ spinal cord white matter come in close apposition with the axolemma, but the regular array of transverse bands between paranodal loops and the axon is absent (Fig. 4B,C, black arrowheads). The most striking paranodal abnormalities often observed in *Cnp-cre/+;Nfasc*$^{Flox/Flox}$ are the overlapping myelin loops of two adjacent myelinating glia that obscure the nodal regions (Fig. 4D, OL). In the example shown in Figure 4D, paranodal loops from the myelin glial segment on the left (labeled OL) overlap the loops of the myelin segment on the right. Additional defects observed in *Cnp-cre/+;Nfasc*$^{Flox/Flox}$ included astrocytic processes that were interposed between the paranodal loops and the axon (Fig. 4D, black arrows) and everted and disorganized paranodal loops that are rarely observed at the paranodes in the wild-type spinal cords (data not shown). These data demonstrate that loss of Nfasc$^{NF155}$ in oligodendrocytes results in paranodal abnormalities and the loss of paranodal axoglial junctions.

## Myelinating Glia-Specific *Nfasc*$^{NF155}$ Mutants Display Organelle Accumulation and Degeneration of Cerebellar Purkinje Axons

Our immunofluorescence analysis of the cerebella from *Cnp-cre/+;Nfasc*$^{Flox/Flox}$ mice revealed Purkinje neuron axonal swellings as previously observed in *Cont* (Boyle et al., 2001), *Caspr*, and *CGT* mutants (Garcia-Fresco et al., 2006). To establish whether Purkinje axons from the *Cnp-cre/+;Nfasc*$^{Flox/Flox}$ mice also undergo axonal degeneration and organelle accumulation, similarly to *Caspr*, *Cont*, and *CGT* mutants, we carried out cross-sections of the wild-type cerebellar white matter and found normal morphology of the myelinated axons with no signs of any vacuolation or degeneration (Fig. 4E, black arrows). In contrast, in the *Cnp-cre/+;Nfasc*$^{Flox/Flox}$ cerebellar white matter, axonal degeneration was very apparent (Fig. 4F, black arrows). Higher magnifications revealed severe structural abnormalities and vacuolation in the degenerating axons (Fig. 4G, black arrows). These characteristics are displayed by axons that are in the terminal stages of degeneration (Palay and Palay, 1974). In an effort to determine the effect of Nfasc$^{NF155}$ deletion on the axonal structure, we performed TEM analysis of the Purkinje axon swellings in *Cnp-cre/+;Nfasc*$^{Flox/Flox}$ mice. We observed large axonal accumulations of organelles, that included mitochondria (m) and smooth endoplasmic

reticulum (SER; Fig. 4H). These axonal accumulations dramatically altered the axonal structure and may ultimately lead to axonal degeneration as observed in Figure 4F,G. Consistently with our immunofluorescence data, we found that the axonal swellings were frequently formed within or in close proximity to the paranodal region, as previously observed in *Caspr* mutants (Einheber et al., 2006; Garcia-Fresco et al., 2006). Taken together, the immunofluorescence and ultrastructural analyses show that loss of Nfasc$^{NF155}$ at the paranodal axoglial junctions leads to paranodal cytoskeletal disorganization and the eventual degeneration of Purkinje axons.

## Ablation of *Nfasc$^{NF155}$* in Adult Myelinating Glia (*Nfasc$^{NF155AD}$*) Reveals Gradual Disorganization of Axonal Domains

The ablation of *Nfasc$^{NF155}$* in myelinating glia during early development showed that *Nfasc$^{NF155}$* is required for the formation of the paranodal axoglial junctions but not myelination per se. However, these studies did not allow us to address how the axoglial junctions and axonal domains are maintained throughout adult life in myelinated axons. To address this question, we took advantage of a tamoxifen inducible-Cre line, developed by Doerflinger et al. (2003), which is specifically expressed in myelinating glia (*Plp-CreER*) to ablate *Nfasc$^{NF155}$* during postnatal development, when axoglial junctions and axonal domains have been well formed and established. P23 *Plp-CreER;Nfasc$^{Flox/Flox}$* mice and age-matched or littermate wild-types were injected with tamoxifen for the next 10 days, until P33 (Fig. 5A, for details see Materials and Methods). The myelinated sciatic nerve fibers and spinal cords of the injected mice were analyzed by immunofluorescence over a period of 10–90 days postinjection for alterations in Nfasc$^{NF155}$ paranodal localization and the domain structure at the nodal/paranodal regions. As shown in Figure 5B, at P33, *Plp–CreER;Nfasc$^{Flox/Flox}$* mice showed normal paranodal localization of Nfasc$^{NF155}$ (green) and Nfasc$^{NF186}$ (red). After 20 days postinjection, Nfasc$^{NF155}$ levels at the paranodes began to decline (Fig. 5C, green). By 40 days postinjection, Nfasc$^{NF155}$ levels were drastically reduced (Fig. 5D, green), and, by postinjection day 60, Nfasc$^{NF155}$ immunoreactivity at the paranodes was essentially absent (Fig. 5E, green). In control mice, which also received tamoxifen, Nfasc$^{NF155}$ localized normally to the paranodes and was indistinguishable from that in the untreated wild types (data not shown). Next, we followed the localization and stability of the axonal paranodal protein Caspr in control and *Plp–CreER;-Nfasc$^{Flox/Flox}$* treated mice. As shown in Figure 5F, at P33, wild-type, control treated mice showed normal localization of Caspr (Fig. 5F, green) and nodal Nfasc$^{NF186}$ (Fig. 5F′, red; also seen in the merged image, Fig. 5F″). In *Plp–CreER;Nfasc$^{Flox/Flox}$* fibers, Caspr immunoreactivity began to decline gradually, to the point at which only traces of paranodal Caspr were seen by 90 days after tamoxifen injection (compare Caspr localization in Fig. 5G–K with F). In contrast, the localization of Nfasc$^{NF186}$ was not affected in *Plp-CreER;Nfasc$^{Flox/Flox}$* fibers (compare Fig. 5G′–K′ with F′). The Caspr immunoreactivity present after 60 and 90 days postinjection was also observed in the nodal region overlapping with Nfasc$^{NF186}$ (Fig. 5J″,K″), suggesting that Nfasc$^{NF155}$ is required to maintain Caspr localization at the paranodes.

We then wanted to determine consequences of loss of Nfasc$^{NF155}$ in adult myelinated fibers on the maintenance of axonal domains, being the juxtaparanodes, the paranodes, and the nodes. As shown in Figure 5L–L‴, wild-type control mice showed distinct localization of $K_v$1.1 at the juxtaparanodes (Fig. 5L, red), Caspr at the paranodes (Fig. 5L′, blue), Nfasc$^{NF186}$ at the nodes (green), and together in the merged image (Fig. 5L‴). In *Plp-CreER;Nfasc$^{Flox/Flox}$* fibers, within 10 days after injection, the juxtaparanodal $K_v$1.1 channels (Fig. 5M, red) began to migrate toward the nodal region. By 30 days postinjection, $K_v$1.1 channels (Fig. 5O, red) had reached closer to the nodal region and began to overlap with the remaining Caspr (Fig. 5O′, blue) at the paranodes. By 60 days after injection, no discrete paranodal region was observed; Caspr immunoreactivity was low, and $K_v$1.1 channels had almost reached the node (merged

image in Fig. 5P″′). By 90 days after injections, $K_v1.1$ channels essentially abutted nodal Nfasc$^{NF186}$, and the paranodal domain was essentially nonexistent (compare Fig. 5M″′–Q″′ with L″′). A quantitative analysis of the paranodal and other domain changes after tamoxifen injection is presented in Table I. Together these data indicate that glial Nfasc$^{NF155}$ is required for the maintenance of paranodal axoglial junctions and that axoglial junctions are critical for the maintenance of the paranodal region and axonal domains in myelinated axons.

As observed in Figure 5CH″,N″′, 20 days after injection, Nfasc$^{NF155}$ and Caspr already show reduced protein levels; therefore, we wanted to determine whether we could identify fibers that were in the process of losing axonal domains, by showing partial overlap of domain markers. As shown in Figure 5R–R″′,S–S″′, as soon as Caspr localization at the paranodes becomes aberrant (Fig. 5R′, blue), $K_v1.1$ begins to migrate toward the paranodes (Fig. 5R′, red). When Caspr localization is intact, for example, in the right paranode (Fig. 5S′, blue), $K_v1.1$ remains at the juxtaparanodes (Fig. 5S, red, and S″′, merged image). The localization of Nfasc$^{NF186}$ (Fig. 5R″,S′, green) is not affected by loss of Nfasc$^{NF155}$. These data suggest that, as soon as axoglial junctions begin to disassemble, axonal domain disorganization ensues, and juxtaparanodal components begin their migration toward the nodal domain.

To determine whether central myelinated axons also follow the same pattern as the peripheral fibers, we analyzed the spinal cord white matter in *Plp-CreER;N-fasc$^{Flox/Flox}$* mice. As shown in Figure 5T–T″′, wild-type controls show normal domain organization, whereas the adult animals that lose Nfasc$^{NF155}$ show gradual disorganization of the axonal domains (Fig. 5U–W″′). One noteworthy feature of the central fibers is that, even in the presence of robust Caspr immunoreactivity at the paranodes (Fig. 5V′,W′, blue), the $K_v1.1$ channels from the juxtaparanodes (Fig. 5V,W, red) persisted in shifting closer to the node (merged images in Fig. 5V″′,W″′). These results suggest that it is the axoglial junctions, not the mere presence of Caspr, that maintains the axonal domains in the myelinated axons. To establish further the time line of loss of Nfasc$^{NF155}$ in adults after injection and the consequences of this on other paranodal proteins, we carried out immunoblot analysis of the spinal cords from age-matched P33 wild-type and *Plp-CreER;Nfasc$^{Flox/Flox}$* tamoxifen-injected animals. As shown in Figure 5X, the levels of Nfasc$^{NF155}$ began to decline steadily by 10 days after injection. By 20 days postinjection, nearly half of the Nfasc$^{NF155}$ protein remained, and nearly none of Nfasc$^{NF155}$ protein could be detected on the immunoblots by postinjection day 60, which is consistent with our immunofluorescence observations (Fig. 5C–E). However, the protein levels of Caspr (Fig. 5Y) and the paranode-enriched protein 4.1B (Fig. 5Z) were not significantly affected. Taken together, these data demonstrate that paranodal axoglial junctions are critical for the maintenance of axonal domains in myelinated axons.

## *Nfasc$^{NF155AD}$* Mutants Display Gradual Loss of Paranodal Axoglial Junctions

Because the light microscopic immunofluorescence analyses in tamoxifen-injected *Plp-CreER;Nfasc$^{Flox/Flox}$* mice revealed disorganization of axonal domains, we wanted to determine the structural changes that occur in the electron-dense transverse bands, or septa, at the para-nodal axoglial junctions. To address this, we carried out electron microscopic examination of spinal cord white matter and sciatic nerves of tamoxifen-injected wild-type and *Plp-CreER;Nfasc$^{Flox/Flox}$* mice. As shown in Figure 6A, P33 wild-type nerves showed normal apposition of paranodal myelin loops with the axolemma, with distinct septa at the interface (Fig. 6, black arrows). The region between the black arrowheads is shown at a higher magnification in Figure 6A, inset. In contrast, the myelinated fibers from *Plp-CreER;Nfasc$^{Flox/Flox}$* 20 days after injection (Fig. 6B), showed atypical transverse bands (septa) from the juxtaparanodal side (left in Fig. 6B), with a loosening of the junctions and diffuse electron-dense structures in the cleft (Fig. 6B, see inset), whereas the paranodal loops toward the nodal side (right in Fig. 6B) maintained distinct transverse bands as seen in the wild

type (Fig. 6A). After 20 days of injection, the mutant fibers showed progressive disorganization of the septal morphology (see Fig. 6, inset) and the axolemma detaching from the myelin loops (Fig. 6C, asterisks). Further analysis of *Plp-CreER;Nfasc*$^{Flox/Flox}$ mice after 40 (Fig. 6D,E) and 90 (Fig. 6F) days of injection, revealed that, by 40 days, some electron density is still present in the myelin/axon cleft at the paranodes, but no presence of intact transverse bands is observed (insets in Fig. 6D,E). By 90 days postinjection, no transverse bands were visible between the myelin loops and the axolemma, and the electron densities noticed at earlier stages had diminished (Fig. 6F, inset). Similarly, we analyzed the sciatic nerves from wild-type and *Plp-CreER;Nfasc*$^{Flox/Flox}$ injected mice. As shown in Figure 6G, wild-type fibers displayed typical morphology of the axoglial transverse bands (Fig. 6G, inset), whereas mutant fibers after 20 days of injection revealed disorganization of axoglial junctions (Fig. 6H). Accordingly, the junctions appeared to disassemble from the juxtaparanodal side (left in Fig. 6H) and progressed gradually toward the node. As shown in Figure 6I at higher magnification, the paranodal loops toward the nodal region side still maintain intact axoglial junctions with their typical morphology. By 90 days after injection, all the axoglial junctions were lost (Fig. 6J, see inset); however, electron densities on the paranodal axonal side were still observed. The presence of these densities indicates that the remnants of the paranodal axonal scaffold that links axoglial junctions to axonal cytoskeleton may remain intact well beyond the disruption of axoglial junctions (Garcia-Fresco et al., 2006). Taken together, the ultrastructural analysis reveals that the paranodal axoglial junctions disorganize gradually, and this disorganization begins from the juxtaparanodal side and progresses gradually toward the nodal side. This conclusion is strengthened by the observations that the juxtaparanodal components, like $K_V1.1$, begin to shift toward the nodal area immediately after axoglial junctions begin to disappear.

## Peripheral Nerve Conduction Is Severely Affected in *Nfasc*$^{NF155}$ and Modestly Affected in *Nfasc*$^{NF155AD}$ Mutants

To determine whether the loss of the paranodal axoglial junctions and/or the altered distribution of ion channels observed in the *Cnp-Cre;Nfasc*$^{Flox/Flox}$, *P0-Cre;Nfasc*$^{Flox/Flox}$, and *Plp-CreER;Nfasc*$^{Flox/Flox}$ affected the electrophysiological properties of peripheral nerves, we performed extracellular recordings from tibial/plantar nerves of litter- or age-matched wild-type (+/+) and mutant mice. Nerves were stimulated at an intensity and duration sufficient to elicit a stable A-component amplitude and latency (for details see Materials and Methods). The electrophysiological measurements from various genotypes at different ages are given in Table II, and representative plots are presented in Figure 7. In *Cnp-Cre;Nfasc*$^{Flox/Flox}$ nerves, conduction velocity (CV) was reduced by 50% at P13 (8.47 m/sec compared with wild-type at 16.83 m/sec; Fig. 7A). At P16.5, *Cnp-Cre;Nfasc*$^{Flox/Flox}$ fibers revealed a CV of 9.5 m/sec compared with a wild-type CV of 17 m/sec (Fig. 7B). At P18, *P0-Cre/+;Nfasc*$^{Flox/Flox}$ nerves had a 41% reduction in CV compared with wild-type (+/+, 17.9; P0-Cre, 12.6; Fig. 7C). In addition to the substantial delay in conduction, *Cnp-cre;Nfasc*$^{Flox/Flox}$ nerves exhibited altered action potential amplitude and duration. *Cnp-Cre;Nfasc*$^{Flox/Flox}$ demonstrated a greater than 50% decrease in amplitude and 50% increase in duration (Fig. 7A,B). This was also observed in *P0-Cre/+;Nfasc*$^{Flox/Flox}$ nerves (Fig. 7C, Table II). In *Plp-CreER;Nfasc*$^{Flox/Flox}$ fibers, the CV was modestly reduced, with a 24% decrease compared with wild-type (Fig. 7D). A further reduction in CV was observed in older *Plp-CreER;Nfasc*$^{Flox/Flox}$ nerves (Fig. 7E, Table II). Taken together, the electrophysiological measurements indicate an important role for paranodal axoglial junctions in ensuring normal action potential propagation in myelinated axons.

## DISCUSSION

The process of myelination and its ultrastructural attributes have long fascinated biologists (Robertson, 1957). Understanding these fundamental processes, and the proteins required for the association of glia with neurons is critical for our understanding of myelin-related neuropathies and how they manifest. Recent work has focused on the molecular composition of axonal domains by biochemical methods, but the role of individual components in axonal domain organization remains elusive (Coetzee et al., 1996; Bhat et al., 2001; Boyle et al., 2001; Sherman et al., 2005; Zonta et al., 2008). Here, by using a glial-specific conditional knockout, we have addressed the role of Nfasc$^{NF155}$ in the organization and maintenance of paranodal axoglial junctions and axonal domains. Our data reveal that Nfasc$^{NF155}$ is a critical component of paranodal junctions and that loss of Nfasc$^{NF155}$ in adult myelinating glia results in the gradual loss of axoglial junctions and concomitant failure to maintain segregated axonal domains. These mutant mice therefore provide a unique animal model for analyzing the role of glial paranodal components in the formation, stabilization, and maintenance of axonal domains in myelinated axons and may further contribute to our understanding of myelin-related diseases (Fig. 8).

### *Nfasc$^{NF155}$* Mutants Display Severe Motor Coordination Defects

Previous work from our laboratory has shown the importance of Caspr/paranodin to paranodal axoglial junction formation (Bhat et al., 2001). Circumstantial evidence suggests that glial Nfasc$^{NF155}$ can associate with Caspr and its axonal partner Cont, but no phenotypic analysis of a glial-specific knockout of Nfasc$^{NF155}$ has been performed, and there is much debate over the exact mechanism(s) of how these proteins associate (Charles et al., 2002; Gollan et al., 2003; Bonnon et al., 2007). Here we find, with glial-specific *Cnp-Cre*, that *Nfasc$^{NF155}$* mutant mice exhibit severe tremors, motor paresis, ataxia, and immobility and die at postnatal day 16 or 17, similarly to both *Caspr* and *Cont* mutant mice (Berglund et al., 1999; Bhat et al., 2001; Boyle et al., 2001). We believe that these neurological defects reflect the function of Nfasc$^{NF155}$ in the myelinating glial cells and not the neuronal Nfasc$^{NF186}$, because *Cnp-Cre* expression has been shown to be restricted to glia within the CNS and PNS (Lappe-Siefke et al., 2003). Additionally, we have shown that Nfasc$^{NF186}$ proteins levels remain unchanged and that the nodal complex remains intact in these animals. These findings indicate for the first time the importance of glial-specific Nfasc$^{NF155}$ in the formation of paranodal axoglial junctions and in coordination of motor function.

### Axon–Glial Interactions at the Nodes and Paranodes of *Nfasc$^{NF155}$* Mutants

The proposed role of glial Nfasc$^{NF155}$ in the organization of the axoglial junctions was suggested by the mutant phenotypes observed in *Nfasc* mutants that lack both Nfasc$^{NF155}$ and Nfasc$^{NF186}$ (Sherman et al., 2005). These mutant mice have severe amyelination and dismyelination as well as a reduction in the levels of myelin-specific proteins, such as MBP and MAG (Zonta et al., 2008). In the current study, we found that glia-specific loss of Nfasc$^{NF155}$ did not alter the myelin ultra-structure but instead resulted in the absence of transverse bands, the hallmark of axoglial junctions. These findings provide formal evidence that Nfasc$^{NF155}$ is a key glial component of axoglial junctions and is consistent with its localization to the paranode (Tait et al., 2000; Charles et al., 2002; Sherman et al., 2005). Interestingly, other paranodal/nodal abnormalities observed in Nfasc$^{NF155}$ mutants are also seen in *Caspr* mutants, suggesting further that loss of either of the paranodal components generates identical phenotypes. Furthermore, the similarities in phenotype between these mutant may be attributed to cytoskeletal abnormalities created by the disruption of the axoglial junctions as seen previously (Einheber et al., 2006; Garcia-Fresco et al., 2006; Sousa and Bhat, 2007).

In the CNS of *Nfasc*$^{NF155}$ mutants, the morphological organization of the paranodal region is severely affected, as evidenced by the appearance of everting and overriding glial paranodal loops. These organizational defects can be attributed to a failure of the paranodal loops to make physical adhesions with the axon in the *Nfasc*$^{NF155}$ mutant mice. Although the paranodal loops of these mutant mice fan outward, the structure of myelin remains unchanged and suggests that the formation and stabilization of the paranode is independent of myelin stabilization. Upon further examination, it was seen that the overriding loops often occluded the node (Fig. 4D), and, although nodal proteins remain localized, such as Nfasc$^{NF186}$, Na channels, and $Ank_G$ (data not shown), the effect of such an obstruction on nodal function remains unknown. The change in the paranodal structure in *Nfasc*$^{NF155}$ mutants may be a result of a change in the trapezoidal geometry of the myelin sheath, as is observed in *Caspr* mutants (Bhat et al., 2001). Other striking abnormalities observed in Nfasc$^{NF155}$ mutants are the axonal swellings and degeneration of cerebellar Purkinje axons (Fig. 2V, W,Fig. 4F–H). In earlier studies, we found that Caspr mutant mice exhibited similar abnormalities. We proposed then that such phenotypes were a result of the disorganization of the paranodal axonal cytoskeleton that results in organelle transport defects at the paranodes and eventual axonal degeneration (Einheber et al., 2006;Garcia-Fresco et al., 2006;Sousa and Bhat, 2007). Our findings indicate further that axoglial junction disruption leads to axonal transport defects and degeneration and indicate a role for the glial cytoskeleton in the maintenance and stabilization of the septate-like junctions as an anchor for the association of glia with axons.

## Keeping Neighbors Apart: Paranodal Junctions and Maintenance of Axonal Domains

A major observation of this study is that the organization of axonal domains in myelinated axons requires myelinating glia-specific expression of Nfasc$^{NF155}$ and that, along with Caspr and Cont, it is able to establish the transverse bands/septa required at the paranodal axon–glial interface. Recent work has suggested that intact paranodal axoglial domains alone, formed by reintroducing Nfasc$^{NF155}$ into a complete *Nfasc* null background, may act to cluster and form the node independent of the neuronal-specific Nfasc$^{NF186}$ (Zonta et al., 2008). Interestingly, these mutant mice were not able to survive past P6, the same expiry as the complete null mice lacking both Nfasc$^{NF155}$ and Nfasc$^{NF186}$. Here we find that $Na^+$ and $K^+$ channels are able to cluster in the absence of the glial Nfasc$^{NF155}$ and intact paranodal junctions. This suggests that these junctions are not required for the clustering of ion channel domains and nodal proteins but instead are likely necessary for their continued segregation (see below). This is consistent with previous observations demonstrating that clustering of nodal components occurs prior to mature paranodal junction formation in the developing PNS (Melendez-Vasquez et al., 2001) and in *CGT* mutant mice that fail to form paranodal axoglial junctions (Coetzee et al., 1996; Dupree et al., 1999). Accordingly, in the absence of the paranodal axoglial junctions in *Nfasc*$^{NF155}$, *Caspr*, *Cont*, and *CGT* mutants, the nodal $Na^+$ and juxtapara-nodal $K^+$ channel domains remain largely segregated, with only occasional overlaps into the nodal region. These phenotypes indicate that distinct molecular interactions, possibly involving specific axonal and glial scaffolding proteins, maintain nodal protein complexes to their respective domains (Peles and Salzer, 2000; Pedraza et al., 2001; Bhat, 2003; Sherman and Brophy, 2005).

To address the importance of axoglial domain stabilization to the segregation of axonal domains, i.e., the node, paranode, and juxtaparanode, in adults we utilized a tamoxifen-inducible *Plp-CreER* to knock out *Nfasc*$^{NF155}$ after stablilization of these domains was complete. Upon observation, we found that, 20 days posttamoxifen injection, Nfasc$^{NF155}$ levels were reduced by 50% and that only after 90 days of injection is near-complete loss of Nfasc$^{NF155}$ seen. These findings indicate that Nfasc$^{NF155}$ is quite stable once it is incorporated into axoglial junctions. In addition, we found that, with increasing time after injection, Caspr staining is gradually reduced and that the juxtaparanodal $K^+$ channels migrated toward the nodal region. The concomitant shift of the clustered juxtaparanodal $K^+$ channels toward the

node suggests that these complexes are mobile and are not anchored by, or within, the axonal/glial cytoskeleton. However, it is unclear why the $K^+$ channels move toward the nodal area instead of diffusing throughout the internode; if it was a simple diffusion in the membrane, then one would expect that they should diffuse in either direction. Interestingly, these new findings are in direct contrast to findings from the *Cnp-Cre;Nfasc*$^{Flox}$ mutant mice shown here, which fail to form paranodal axoglial junctions but still maintain segregated nodal and juxtaparanodal domains. These results indicate that two independent functions exist to segregate and maintain axonal domains during development and in mature animals. During development, each axonal domain is assembled and stabilized independently of the other and thus retains its anchorage at the respective domain, whereas, in the adult, maintenance of the domains requires the paranode to act as a fence to segregate the domains. This suggests that, with time, as these animals progressively lose the paranodal axoglial junctions, that both the juxtaparanodal complex and the nodal complex may diffuse throughout the internodes, which may lead to severe depolarization and abnormal saltatory conduction.

## Conduction Velocity and the Role of Paranodal Axoglial Junctions

Electrophysiological data on *Nfasc*$^{NF155}$ mutant mice generated during embryonic development reveal that population nerve CVs are severely reduced in peripheral nerve fibers. These defects may reflect changes in the properties of fast-conducting myelinated fibers and may also be caused by a conduction block in a subset of fibers and/or slower propagation in the remaining fibers. Another possibility for the weakened CVs observed in *Nfasc*$^{NF155}$ mutant mice is that the disorganized paranodal region may cause current leakage into the periaxonal space. Leakage of the current may in turn increase the capacitance of the axonal membrane, leading to slow action potential propagation (Chiu and Ritchie, 1980; Boyle et al., 2001). Interestingly, it might be expected that in the adult *Nfasc*$^{NF155}$ mutant mice CVs would be slowed concomitantly with the degradation of axoglial junctions; however, we found that both the CV and the CAP peak-to-peak amplitudes were not dramatically altered in the mutant mice compared with control mice of the same age. These results were seen even in mice examined 6 months postinjection that had near-complete loss of Nfasc$^{NF155}$ protein levels and disassembled paranodal junctions (Fig. 7). It is not clear why the loss of axoglial junctions during adult stages has a less dramatic effect on the electrophysiological properties of the peripheral nerve fibers than loss in early developmental stages. One possibility is that many structural features are maintained in adult mutant nerves that allow the conduction of action potentials at near-normal or at a slightly reduced velocity. Alternatively, it could be that different classes of fibers in these adult nerves conduct differently and what we observed is a summation of all the fibers. It is unlikely that the reduced change in CVs is due to the injection and variability of its penetration to all glial cells, insofar as our quantitative measurements revealed that greater than 90–95% of the Schwann cells lost Nfasc$^{NF155}$ after 10 days of tamoxifen treatment (Table I), so the modest changes in CV and amplitude in adult fibers may be due to the structural integrity of the nerve fibers and slow disorganization of the axonal domains over time. It would be interesting to see how the *Nfasc*$^{NF155}$ mutant mice CVs faired through extended time, in that it has been shown that human demyelinating neuropathies, where axonal domains are compromised, such as multiple sclerosis and Charcot-Marie-Tooth disease, CVs are severely reduced (Nicholson, 1999; Wolswijk and Balesar, 2003; Coman et al., 2006). Further studies on *Nfasc*$^{NF155}$ mutant mice may reveal more similarities to human neurological disorders and provide a system for studying human disease. In summary, we have demonstrated that glial Nfasc$^{NF155}$ is critical for the formation of the paranodal axoglial junctions and that these junctions are central to the organization and maintenance of the axonal domains in myelinated axons.

## Acknowledgments

We are immensely grateful to Drs. Brian Popko (University of Chicago), Klaus Nave (Max Planck Institute of Experimental Medicine), and Laura Feltri (San Rafaele Scientific Institute, Italy) for generously sharing their Cre-expressing mouse strains. Our special thanks go to Dr. Edward Perl for his generous support and advice and for making his electrophysiology facility available to us to perform nerve conduction studies. We also thank Dr. G. Garcia-Fresco for drawing the schematics in Figure 8; Drs. W. Snider, J. Zhong, J. Salzer, and A. Gow for reagents; Drs. A. Fanning and S. Banerjee for comments on the manuscript; and members of the Bhat laboratory for valuable discussions. The electron microscopy was performed at the VCU and supported, in part, with funding from NIH-NINDS Center core grant 5P30NS047463.

Contract grant sponsor: National Institutes of Health; Contract grant number: GM63074; Contract grant number: NS050356; Contract grant sponsor: National MS Society; Contract grant sponsor: State of North Carolina (to M.A.B.).

## REFERENCES

Arroyo EJ, Xu YT, Zhou L, Messing A, Peles E, Chiu SY, Scherer SS. Myelinating Schwann cells determine the internodal localization of $K_V1.1$, $K_V1.2$, $K_V$beta2, and Caspr. J Neurocytol 1999;28:333–347. [PubMed: 10739575]

Banerjee S, Pillai AM, Paik R, Li J, Bhat MA. Axonal ensheathment and septate junction formation in the peripheral nervous system of *Drosophila*. J Neurosci 2006a;26:3319–3329. [PubMed: 16554482]

Banerjee S, Sousa AD, Bhat MA. Organization and function of septate junctions: an evolutionary perspective. Cell Biochem Biophys 2006b;46:65–77. [PubMed: 16943624]

Berglund EO, Murai KK, Fredette B, Sekerkova G, Marturano B, Weber L, Mugnaini E, Ranscht B. Ataxia and abnormal cerebellar microorganization in mice with ablated contactin gene expression. Neuron 1999;24:739–750. [PubMed: 10595523]

Bhat MA. Molecular organization of axoglial junctions. Curr Opin Neurobiol 2003;13:552–559. [PubMed: 14630217]

Bhat MA, Izaddoost S, Lu Y, Cho KO, Choi KW, Bellen HJ. Discs Lost, a novel multi-PDZ domain protein, establishes and maintains epithelial polarity. Cell 1999;96:833–845. [PubMed: 10102271]

Bhat MA, Rios JC, Lu Y, Garcia-Fresco GP, Ching W, St. Martin M, Li J, Einheber S, Chesler M, Rosenbluth J, Salzer JL, Bellen HJ. Axon–glia interactions and the domain organization of myelinated axons requires neurexin IV/Caspr/paranodin. Neuron 2001;30:369–383. [PubMed: 11395000]

Bonnon C, Bel C, Goutebroze L, Maigret B, Girault JA, Faivre-Sarrailh C. PGY repeats and N-glycans govern the trafficking of paranodin and its selective association with contactin and neurofascin-155. Mol Biol Cell 2007;18:229–241. [PubMed: 17093057]

Boyle ME, Berglund EO, Murai KK, Weber L, Peles E, Ranscht B. Contactin orchestrates assembly of the septate-like junctions at the paranode in myelinated peripheral nerve. Neuron 2001;30:385–397. [PubMed: 11395001]

Charles P, Tait S, Faivre-Sarrailh C, Barbin G, Gunn-Moore F, Denisenko-Nehrbass N, Guennoc AM, Girault JA, Brophy PJ, Lubetzki C. Neurofascin is a glial receptor for the paranodin/Caspr-contactin axonal complex at the axoglial junction. Curr Biol 2002;12:217–220. [PubMed: 11839274]

Chiu SY, Ritchie JM. Potassium channels in nodal and internodal axonal membrane of mammalian myelinated fibres. Nature 1980;284:170–171. [PubMed: 6244497]

Coetzee T, Fujita N, Dupree J, Shi R, Blight A, Suzuki K, Popko B. Myelination in the absence of galactocerebroside and sulfatide: normal structure with abnormal function and regional instability. Cell 1996;86:209–219. [PubMed: 8706126]

Coman I, Aigrot MS, Seilhean D, Reynolds R, Girault JA, Zalc B, Lubetzki C. Nodal, paranodal and juxtaparanodal axonal proteins during demyelination and remyelination in multiple sclerosis. Brain 2006;129:3186–3195. [PubMed: 16766541]

Davis JQ, Lambert S, Bennett V. Molecular composition of the node of Ranvier: identification of ankyrin-binding cell adhesion molecules neurofascin (mucin$^+$/third FNIII domain$^-$) and NrCAM at nodal axon segments. J Cell Biol 1996;135:1355–1367. [PubMed: 8947556]

Denisenko-Nehrbass N, Oguievetskaia K, Goutebroze L, Galvez T, Yamakawa H, Ohara O, Carnaud M, Girault JA. Protein 4.1B associates with both Caspr/paranodin and Caspr2 at paranodes and juxtaparanodes of myelinated fibres. Eur J Neurosci 2003;17:411–416. [PubMed: 12542678]

Doerflinger NH, Macklin WB, Popko B. Inducible site-specific recombination in myelinating cells. Genesis 2003;35:63–72. [PubMed: 12481300]

Dupree JL, Girault JA, Popko B. Axoglial interactions regulate the localization of axonal paranodal proteins. J Cell Biol 1999;147:1145–1152. [PubMed: 10601330]

Einheber S, Zanazzi G, Ching W, Scherer S, Milner TA, Peles E, Salzer JL. The axonal membrane protein Caspr, a homologue of neurexin IV, is a component of the septate-like paranodal junctions that assemble during myelination. J Cell Biol 1997;139:1495–1506. [PubMed: 9396755]

Einheber S, Bhat MA, Salzer JL. Disrupted axoglial junctions result in accumulation of abnormal mitochondria at nodes of Ranvier. Neuron Glia Biol 2006;2:165–174. [PubMed: 17460780]

Feltri ML, D'Antonio M, Previtali S, Fasolini M, Messing A, Wrabetz L. P0-Cre transgenic mice for inactivation of adhesion molecules in Schwann cells. Ann N Y Acad Sci 1999;883:116–123. [PubMed: 10586237]

Garcia-Fresco GP, Sousa AD, Pillai AM, Moy SS, Crawley JN, Tessarollo L, Dupree JL, Bhat MA. Disruption of axoglial junctions causes cytoskeletal disorganization and degeneration of Purkinje neuron axons. Proc Natl Acad Sci USA 2006;103:5137–5142. [PubMed: 16551741]

Gasser HS, Grundfest H. Axon diameters in relation to the spike dimensions and the conduction velocity in mammalian A fibers. Am J Physiol 1939;127:22.

Gollan L, Salomon D, Salzer JL, Peles E. Caspr regulates the processing of contactin and inhibits its binding to neurofascin. J Cell Biol 2003;163:1213–1218. [PubMed: 14676309]

Griffiths I, Klugmann M, Anderson T, Yool D, Thomson C, Schwab MH, Schneider A, Zimmermann F, McCulloch M, Nadon N, Nave KA. Axonal swellings and degeneration in mice lacking the major proteolipid of myelin. Science 1998;280:1610–1613. [PubMed: 9616125]

Hartline DK, Colman DR. Rapid conduction and the evolution of giant axons and myelinated fibers. Curr Biol 2007;17:R29–R35. [PubMed: 17208176]

Ishibashi T, Dupree JL, Ikenaka K, Hirahara Y, Honke K, Peles E, Popko B, Suzuki K, Nishino H, Baba H. A myelin galactolipid, sulfatide, is essential for maintenance of ion channels on myelinated axon but not essential for initial cluster formation. J Neurosci 2002;22:6507–6514. [PubMed: 12151530]

Lappe-Siefke C, Goebbels S, Gravel M, Nicksch E, Lee J, Braun PE, Griffiths IR, Nave KA. Disruption of Cnp1 uncouples oligodendroglial functions in axonal support and myelination. Nat Genet 2003;33:366–374. [PubMed: 12590258]

Liu P, Jenkins NA, Copeland NG. A highly efficient recombineering-based method for generating conditional knockout mutations. Genome Res 2003;13:476–484. [PubMed: 12618378]

Melendez-Vasquez CV, Rios JC, Zanazzi G, Lambert S, Bretscher A, Salzer JL. Nodes of Ranvier form in association with ezrin-radixin-moesin (ERM)-positive Schwann cell processes. Proc Natl Acad Sci USA 2001;98:1235–1240. [PubMed: 11158623]

Menegoz M, Gaspar P, Le Bert M, Galvez T, Burgaya F, Palfrey C, Ezan P, Arnos F, Girault JA. Paranodin, a glycoprotein of neuronal paranodal membranes. Neuron 1997;19:319–331. [PubMed: 9292722]

Nicholson GA. Mutation testing in Charcot-Marie-Tooth neuropathy. Ann N Y Acad Sci 1999;883:383–388. [PubMed: 10586262]

Ogawa Y, Schafer DP, Horresh I, Bar V, Hales K, Yang Y, Susuki K, Peles E, Stankewich MC, Rasband MN. Spectrins and ankyrinB constitute a specialized paranodal cytoskeleton. J Neurosci 2006;26:5230–5239. [PubMed: 16687515]

Palay, SL.; Palay, VC. Cerebellar cortex. New York: Springer-Verlag; 1974.

Pedraza L, Huang JK, Colman DR. Organizing principles of the axoglial apparatus. Neuron 2001;30:335–344. [PubMed: 11394997]

Peles E, Salzer JL. Molecular domains of myelinated axons. Curr Opin Neurobiol 2000;10:558–565. [PubMed: 11084317]

Peles E, Nativ M, Lustig M, Grumet M, Schilling J, Martinez R, Plowman GD, Schlessinger J. Identification of a novel contactin-associated transmembrane receptor with multiple domains implicated in protein–protein interactions. EMBO J 1997;16:978–988. [PubMed: 9118959]

Pillai AM, Garcia-Fresco GP, Sousa AD, Dupree JL, Philpot BD, Bhat MA. No effect of genetic deletion of contactin-associated protein (CASPR) on axonal orientation and synaptic plasticity. J Neurosci Res 2007;85:2318–2331. [PubMed: 17549747]

Rasband MN, Tayler J, Kaga Y, Yang Y, Lappe-Siefke C, Nave KA, Bansal R. CNP is required for maintenance of axon–glia interactions at nodes of Ranvier in the CNS. Glia 2005;50:86–90. [PubMed: 15657937]

Reeh PW. Sensory receptors in mammalian skin in an in vitro preparation. Neurosci Lett 1986;66:141–146. [PubMed: 3725179]

Rios JC, Melendez-Vasquez CV, Einheber S, Lustig M, Grumet M, Hemperly J, Peles E, Salzer JL. Contactin-associated protein (Caspr) and contactin form a complex that is targeted to the paranodal junctions during myelination. J Neurosci 2000;20:8354–8364. [PubMed: 11069942]

Robertson JD. The ultrastructure of nodes of Ranvier in frog nerve fibres. J Physiol 1957;137:8P–9P. [PubMed: 13439596]

Salzer JL. Polarized domains of myelinated axons. Neuron 2003;40:297–318. [PubMed: 14556710]

Schafer DP, Custer AW, Shrager P, Rasband MN. Early events in node of Ranvier formation during myelination and remyelination in the PNS. Neuron Glia Biol 2006;2:69–79. [PubMed: 16652168]

Sherman DL, Brophy PJ. Mechanisms of axon ensheathment and myelin growth. Nat Rev Neurosci 2005;6:683–690. [PubMed: 16136172]

Sherman DL, Tait S, Melrose S, Johnson R, Zonta B, Court FA, Macklin WB, Meek S, Smith AJ, Cottrell DF, Brophy PJ. Neurofascins are required to establish axonal domains for saltatory conduction. Neuron 2005;48:737–742. [PubMed: 16337912]

Sousa AD, Bhat MA. Cytoskeletal transition at the paranodes: the Achilles' heel of myelinated axons. Neuron Glia Biol 2007;3:169–178. [PubMed: 18372928]

Southwood C, He C, Garbern J, Kamholz J, Arroyo E, Gow A. CNS myelin paranodes require Nkx6–2 homeoprotein transcriptional activity for normal structure. J Neurosci 2004;24:11215–11225. [PubMed: 15601927]

Stampfli R. A new method for measuring membrane potentials with external electrodes. Experientia 1954;10:508–509. [PubMed: 14353097]

Tait S, Gunn-Moore F, Collinson JM, Huang J, Lubetzki C, Pedraza L, Sherman DL, Colman DR, Brophy PJ. An oligodendrocyte cell adhesion molecule at the site of assembly of the paranodal axoglial junction. J Cell Biol 2000;150:657–666. [PubMed: 10931875]

Wolswijk G, Balesar R. Changes in the expression and localization of the paranodal protein Caspr on axons in chronic multiple sclerosis. Brain 2003;126:1638–1649. [PubMed: 12805111]

Zonta B, Tait S, Melrose S, Anderson H, Harroch S, Higginson J, Sherman DL, Brophy PJ. Glial and neuronal isoforms of Neurofascin have distinct roles in the assembly of nodes of Ranvier in the central nervous system. J Cell Biol 2008;181:1169–1177. [PubMed: 18573915]

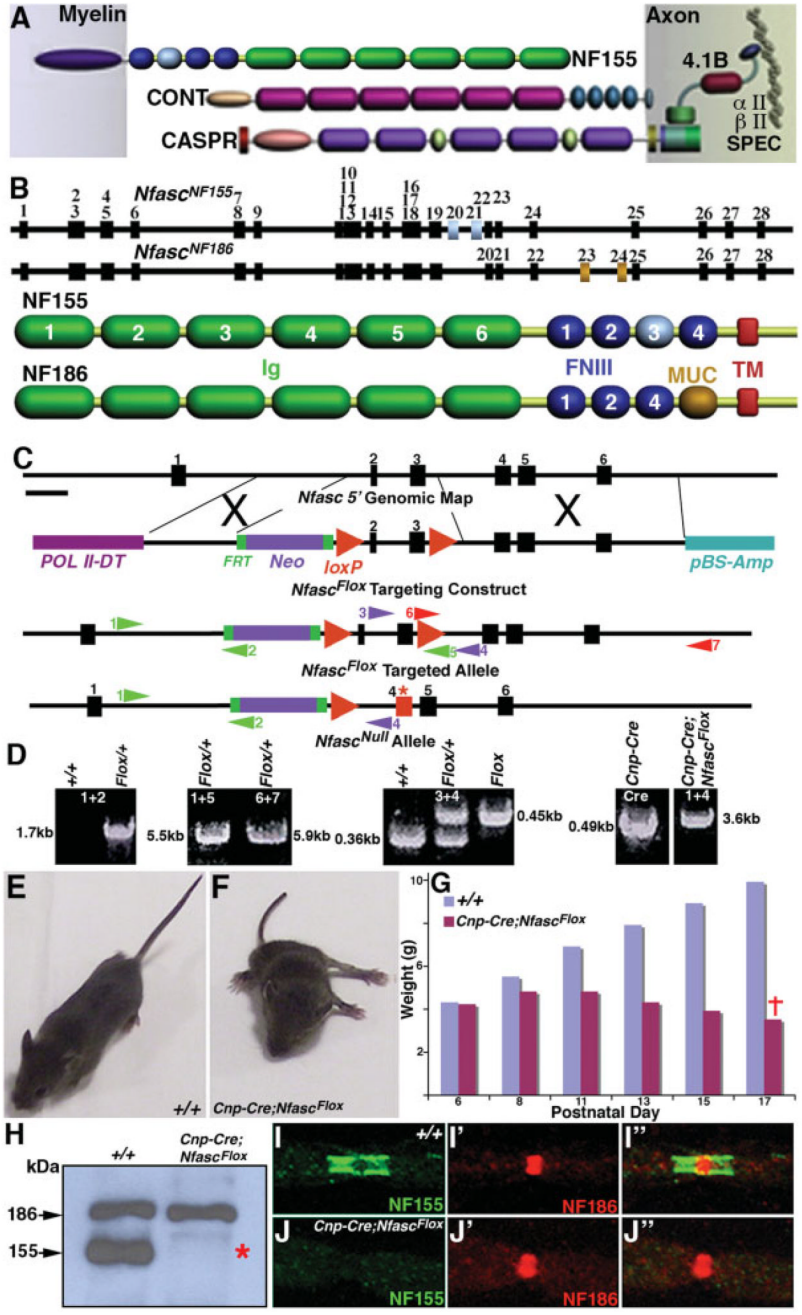


**Fig. 1.**

Conditional ablation of *Nfasc*$^{NF155}$ in myelinating glia. **A**: Main molecular components of the paranodal axoglial junctional complex with Nfasc$^{NF155}$ on the myelin side and Caspr and Cont on the axonal side. Additional paranode-enriched proteins that either interact or are associated with Caspr protein complex are also shown. **B**: Exon/intron structure of two major *Nfasc* transcripts expressed either in myelinating glia, *Nfasc*$^{NF155}$, or in neurons, *Nfasc*$^{NF186}$. The glial transcript contains unique exons numbered 20 and 21 encoding the third FNIII domain (colored in gray) in Nfasc$^{NF155}$. The neuronal transcript contains unique exons numbered 23 and 24 that encode a mucin domain (colored in dark gold) in Nfasc$^{NF186}$. **C**: Exon/intron structure in the 5′ region of *Nfasc* showing exons 1–6. The exon that encodes the putative

initiation methionine, based on the reported protein sequences of Nfasc$^{NF155}$ and Nfasc$^{NF186}$, is referred to here as *exon 1*. To generate a null mutation in *Nfasc*, a targeting construct was engineered by using the BAC recombineering technology (Liu et al., 2003). A 1.9-kb fragment upstream of exon 2 was inserted between *Pol*II-DT and *FRT-Neo-FRT-loxP* cassette, and a second *loxP* site was inserted downstream of exon 3. This targeting construct, *Nfasc$^{Flox}$*, was used for ES cell transformation. The targeted ES cell clones were identified by PCR amplification with primer sets depicted on the map. Upon Cre-mediated recombination, ~2.1 kb of genomic DNA containing exons 2 and 3 was deleted, resulting in translation termination in exon 4 (red asterisk) that generated the *Nfasc$^{Null}$* allele. **D**: PCR amplification strategies using color-coded primer sets with numbers to distinguish various genotypes. Wild-type (+/+), *Nfasc$^{Flox}$*/+ (*Flox*/+), and *Nfasc$^{Flox/Flox}$* (*Flox*) were distinguished by the primer sets 3 and 4. Upon Cre-mediated deletion of ~2.1 kb of the genomic DNA containing exons 2 and 3, the primer sets 1 and 4 amplified a 3.6-kb fragment in *Cnp-Cre;Nfasc$^{Flox}$*. **E**: Appearance of a wild-type (+/+) mouse at P17 with normal walking posture. **F**: A littermate *Cnp-Cre;Nfasc$^{Flox}$* mouse is less than half the weight (3.8 vs. 9.8 g) of the wild-type mouse and exhibits a characteristic wide base in the hind limbs. The mutant mice are severely hypomotile and are not able to walk forward. **G**: The chart illustrates the weights of wild-type (+/+) and *Cnp-Cre;Nfasc$^{Flox}$* male littermates. Both genotypes at P6 have identical weight (4.2 g). The weight of the mutant mice progressively declines, and all die before reaching P18. The weights shown are mean of four animals in each age group. **H**: Immunoblot analysis of spinal cord protein lysates from wild-type (+/+) and *Cnp-Cre;Nfasc$^{Flox}$* mice using NFCT antibodies. The wild-type lysates show two predominant protein bands migrating at 186 and 155 kDa corresponding to Nfasc$^{NF186}$ and Nfasc$^{NF155}$, respectively. The *Cnp-Cre;Nfasc$^{Flox}$* mutant lysates contain the 186-kDa band, corresponding to Nfasc$^{NF186}$, and lack the 155-kDa band, demonstrating specific loss of Nfasc$^{NF155}$ in *Cnp-Cre;Nfasc $^{Flox}$* mutant mice (red asterisk). *I–I″*: Immunofluorescence analysis of the sciatic nerves from wild-type (+/+) mice showing paranodal localization of Nfasc$^{NF155}$ (I, green) and nodal localization of Nfasc$^{NF186}$ (I′, red) and together in the merged image (I″). **J–J″**: Immunofluorescence analysis of the sciatic nerves from Cnp-Cre;Nfasc$^{Flox}$ mutants showing loss of paranodal Nfasc$^{NF155}$ (J, green) but normal localization of nodal Nfasc$^{NF186}$ (J′, red) and together in the merged image (J″) demonstrating specific loss of Nfasc$^{NF155}$.

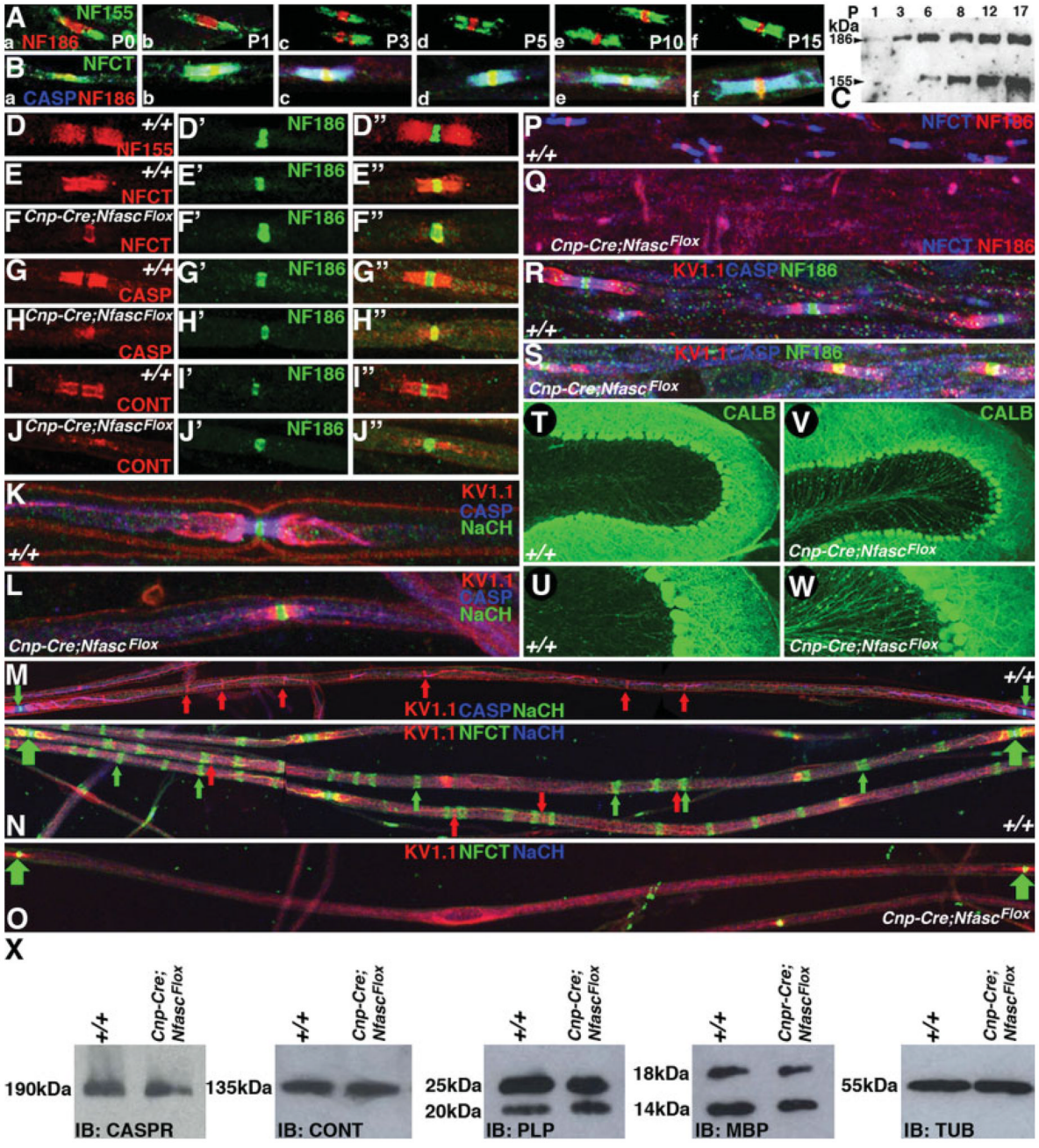


**Fig. 2.**

Nfasc$^{NF155}$ mutants display abnormal localization of the paranodal proteins and disorganization of axonal domains. **A**: Immunofluorescence of sciatic nerve fibers depicting the postnatal expression profile of two *Nfasc* encoded protein isoforms using antibodies generated against unique domains of Nfasc$^{NF155}$ and Nfasc$^{NF186}$. Nfasc$^{NF155}$ localizes to developing paranodes (Aa–f, green), and Nfasc$^{NF186}$ localizes to the nodes (Aa–f, red). **B**: Immunofluorescence of sciatic nerve fibers using antibodies against both Nfasc$^{NF155}$ and Nfasc$^{NF186}$ (Ba–f, NFCT, green), against Caspr (CASP, blue), and against Nfasc$^{NF186}$ (red) during postnatal development, as in Aa–f. The paranodal colocalization of Nfasc$^{NF155}$ and Caspr is seen throughout postnatal development. **C**: Immunoblot of spinal cord lysates for a

postnatal expression profile of Nfasc$^{NF155}$ (155 kDa) and Nfasc$^{NF186}$ (186 kDa) using NFCT antibodies that recognize both isoforms. Nfasc$^{NF186}$ levels are relatively higher than Nfasc$^{NF155}$ levels until P3. However, longer exposures of the blots reveal the presence of Nfasc$^{NF155}$ at P1 as well. Equal amounts of the total protein were loaded for these immunoblots and confirmed with antitubulin immunoblots (data not shown). **D–D″**: Wild-type sciatic nerve fibers immunostained against paranodal Nfasc$^{NF155}$ (D, red) and Nfasc$^{NF186}$ (D′, green) and in a merged image (D″). **E–E″**: Wild-type sciatic nerve fibers immunostained against NFCT antibodies (E, Nfasc$^{NF155}$/Nfasc$^{NF186}$, red) and nodal Nfasc$^{NF186}$ (E′, green) and in a merged image (D″). Note that NFCT recognizes both Nfasc$^{NF155}$ and Nfasc$^{NF186}$. Nfasc$^{NF186}$ immunoreactivity by the two antibodies appears yellow in the merged panel (E″). **F–F″**: *Cnp-Cre;Nfasc$^{Flox}$* sciatic nerve fibers immunostained with NFCT antibodies (F, Nfasc$^{NF155}$/Nfasc$^{NF186}$, red) and nodal Nfasc$^{NF186}$ (F′, green) and in a merged image (F″). Note that Nfasc$^{NF155}$ is absent from the paranodes, whereas Nfasc$^{NF186}$ immunoreactivity with two different antibodies remains unaffected. **G–G″**: Wild-type sciatic nerve fibers immunostained against paranodal Caspr (G, CASP, red) and nodal Nfasc$^{NF186}$ (G′, green) and in a merged image (G″). **H–H″**: *Cnp-Cre;Nfasc$^{Flox}$* sciatic nerve fibers immunostained against paranodal Caspr (red) and nodal Nfasc$^{NF186}$ (F′, green) and in a merged image (H″). Note that Caspr fails to localize at the paranodes and is diffusely present around the nodal/paranodal region, occasionally showing overlap with Nfasc$^{NF186}$ (H″). **I–I″**: Wild-type sciatic nerve fibers immunostained against paranodal Cont (I, red) and nodal Nfasc$^{NF186}$ (I′, green) and in a merged image (I″). **J–J″**: *Cnp-Cre;Nfasc $^{Flox}$* sciatic nerve fibers immunostained against paranodal Cont (J, red) and nodal Nfasc$^{NF186}$ (J′, green) and in a merged image (J″). Note that Cont fails to localize at the paranodes and is diffusely present around the nodal/paranodal region. **K**: Wild-type sciatic nerve fibers triply immunostained against the juxtaparanodal potassium channels ($K_v$1.1, red), Caspr (blue), and nodal sodium channels (NaCH, green). Note that these proteins localize to distinct domains. **L**: *Cnp-Cre;Nfasc$^{Flox}$* sciatic nerve fibers triply immunostained against the juxtaparanodal potassium channels (red), Caspr (blue), and nodal sodium channels (green). Note that the juxtaparanodal $K^+$ channels fail to segregate from the nodal $Na^+$ channels. Caspr (blue) immunoreactivity is diffusely present along the axon. **M**: Wild-type sciatic nerve fibers triply immunostained against $Na^+$ channels to highlight nodes (green arrows) flanking the entire internodal region. Caspr (blue) highlights the paranodes. Note the $K^+$ channel localization at the Schmidt-Lanterman incisures and the inner mesaxon (red arrows). **N**: Wild-type sciatic nerve fibers triply immunostained against $Na^+$ channels (blue) and NFCT highlight two contiguous nodes (green arrows). Note that Nfasc$^{NF155}$ labels the Schmidt-Lanterman incisures (NFCT, green arrows) as well as $K_v$1.1 (red arrows). Nfasc$^{NF155}$ and $K_v$1.1 immunoreactivity is always observed either overlapping with or in close proximity to each other. **O**: *Cnp-Cre;Nfasc$^{Flox}$* sciatic nerve fibers triply immunostained against $Na^+$ channels (NaCH, blue) and Nfasc$^{NF186}$ (green) highlight two nodes (green arrows). Between the two nodes, the internodal region shows no Nfasc$^{NF155}$ immunoreactivity. $K_v$1.1 (red) highlights juxtaparanodal regions and is also diffusely present along the axon. **P**: Wild-type spinal cord sections against NFCT (blue) and Nfasc$^{NF186}$ (red). Nfasc$^{NF155}$ is in blue and the nodal Nfasc$^{NF186}$ is in pink, as both antibodies recognize Nfasc$^{NF186}$. **Q**: *Cnp-Cre;Nfasc$^{Flox}$* spinal cord sections stained against NFCT (blue) and Nfasc$^{NF186}$ (red). Nfasc$^{NF155}$ (blue) is absent, but the nodal Nfasc$^{NF186}$ is present and indistinguishable from the wild-type Nfasc$^{NF186}$ (as in Q). **R**: Wild-type spinal cord sections stained against axonal domain markers $K_v$1.1 (red), Caspr (blue), and Nfasc$^{NF186}$ (green) show proper domain organization. **S**: *Cnp-Cre;Nfasc$^{Flox}$* spinal cord sections stained against axonal domain markers $K_v$1.1 (red), Caspr (blue), and Nfasc$^{NF186}$ (green) show abnormal domain organization. The paranodal domain is compromised and $K_v$1.1 is almost overlapping with nodal Nfasc$^{NF186}$, which is never observed in the wild-type animals. **T,U**: A wild-type cerebellar loop immunostained against calbindin (green) to reveal anatomical organization of various layers and cerebellar white matter at low magnification (T) and at a higher magnification (U) with a focus on the Purkinje axons. **V,W**: A *Cnp-Cre;Nfasc$^{Flox}$* cerebellar loop immunostained

against calbindin (green) to reveal the anatomical organization of various layers and cerebellar white matter at low magnification (V) and at a higher magnification (W) with a focus on the Purkinje axons. Note the Purkinje axonal swellings as green dots on the axons, which are never observed in the wild-type animals. **X**: Immunoblots of protein lysates from wild-type (+/+) and *Cnp-Cre;Nfasc*$^{Flox}$ brains against paranodal proteins (Caspr, Cont) and myelin proteins (PLP, MBP) did not shown any significant differences in the levels of the these proteins. Identical blots were probed with mouse antitubulin as a loading control.

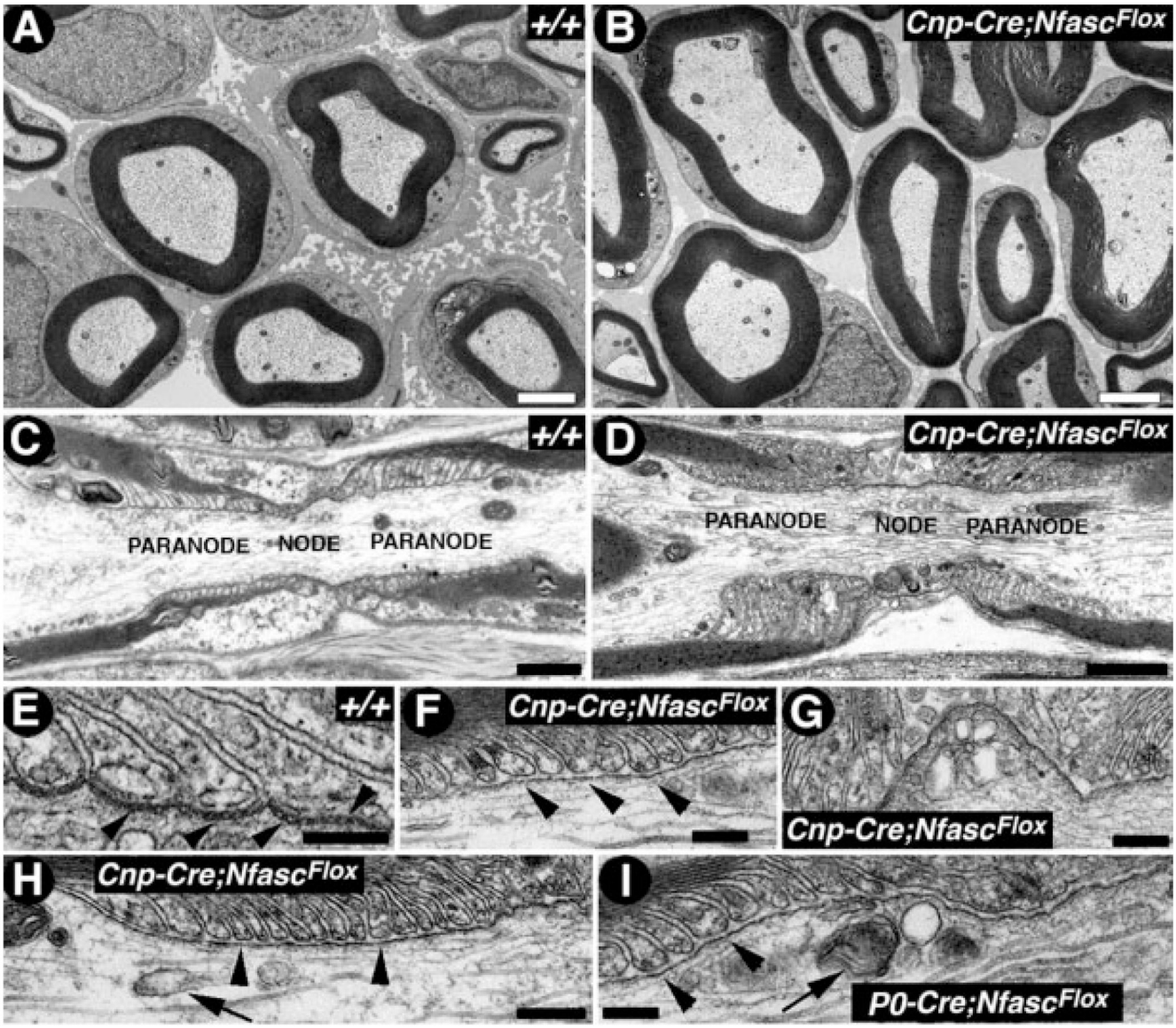


**Fig. 3.**

*Nfasc*$^{NF155}$ mutants fail to form paranodal axoglial junctions. **A,B**: Electron micrographs of cross-sections of sciatic nerves from P17 littermates wild-type (A, +/+) and *Cnp-Cre;Nfasc*$^{Flox}$ (B) mice. No significant changes in myelin thickness or axon diameter were noticed between these genotypes. **C,D**: Electron micrographs of longitudinal sections through the nodal/paranodal region of sciatic nerves from P17 wild-type (C, +/+) and *Cnp-Cre;Nfasc*$^{Flox}$ mutants (D). At low magnification, the paranodal myelin loops in the mutant fibers are properly arrayed and show normal profiles as in the wild-type. **E**: Electron micrograph of a longitudinal section through the paranodal region of a sciatic nerve myelinated axon from a P17 wild-type (+/+) mouse shows paranodal loops tightly apposed to and indenting the axon, the characteristic transverse bands are also apparent (black arrowheads). **F,H**: Electron micrographs of longitudinal sections through the paranodal region of sciatic nerve myelinated axons from a P17 *Cnp-Cre;Nfasc* $^{Flox}$ mutant mouse. Note that the paranodal loops come in close apposition and face the axon but fail to form the transverse bands or septa with

the axolemma. **G**: Electron micrograph of the nodal region from a *Cnp-Cre;Nfasc*$^{Flox}$ mutant sciatic nerve fiber showing organelle build up, forming nodal pockets. Such abnormalities have been previously observed in *Caspr* mutants with disrupted axoglial junctions (Einheber et al., 2006). **I**: Electron micrograph of a longitudinal section through the paranodal region of a sciatic nerve myelinated axon from a P17 *P0-Cre;Nfasc*$^{Flox}$ mutant mouse. These mutant fibers display same phenotypes in the PNS as the *Cnp-Cre;Nfasc*$^{Flox}$ mutant fibers. Scale bars = 2 μm in A, B; 1 μm in C, D; 0.2 μm in E–I.

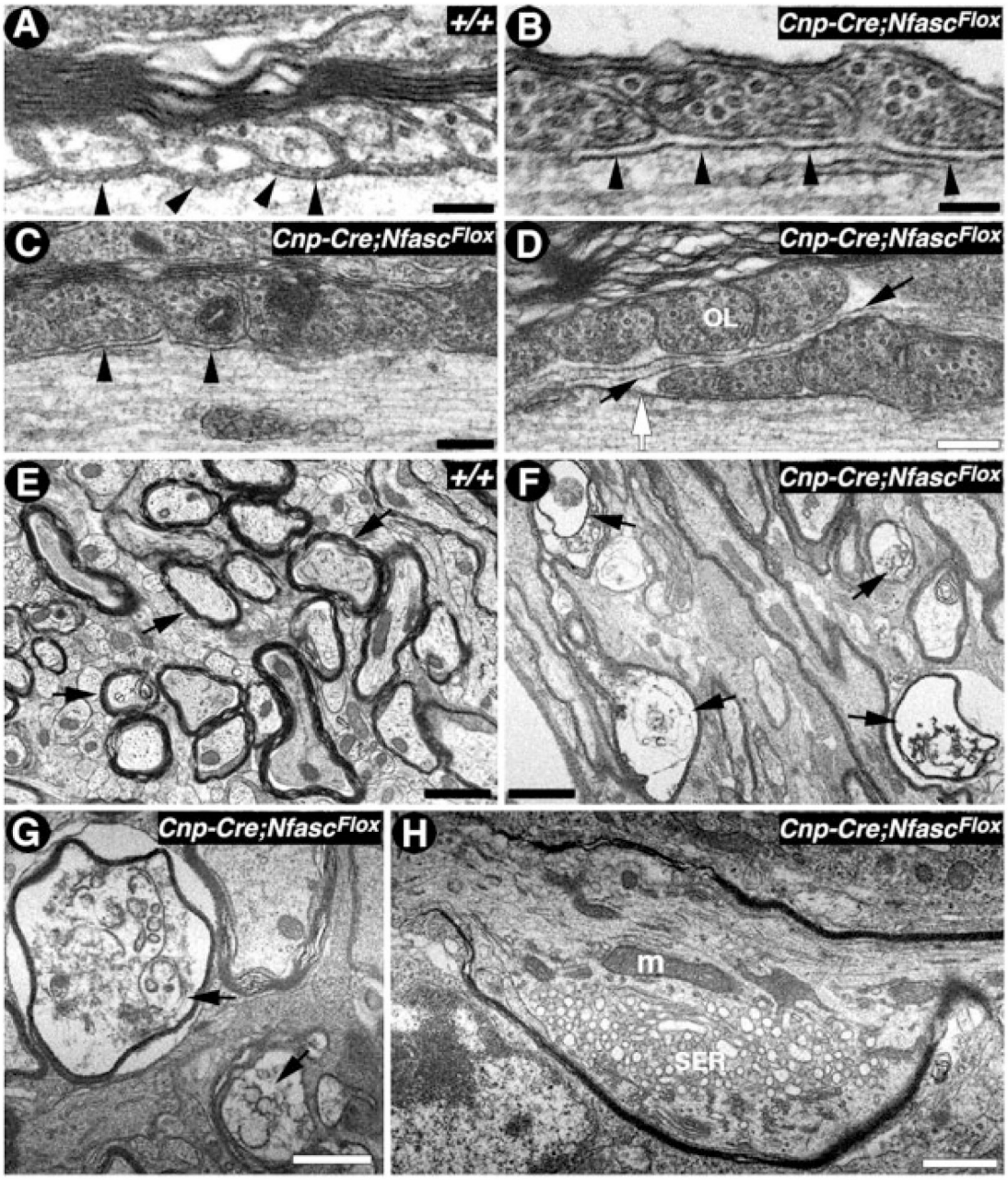


**Fig. 4.**

*Nfasc*$^{NF155}$ mutants display organelle accumulation and Purkinje neuron axonal degeneration. **A**: Electron micrograph of the paranodal region of a spinal cord myelinated fiber from P17 wild-type (+/+) mouse shows paranodal loops tightly apposed to and indenting the axon; the characteristic transverse bands are apparent (black arrowheads). **B–D**: Electron micrographs of the paranodal regions of spinal cord myelinated fibers from P17 *Cnp-Cre;Nfasc*$^{Flox}$ mutants show closely apposed paranodal loops but a lack of transverse bands (B,C, black arrowheads). In D, paranodal loops from one myelin segment override loops (OL) from another segment, thereby occluding the node (white arrow). An astrocytic process has entered the gap between the overriding myelin loops (black arrows). **E**: Electron micrographs of cerebellar white matter

from P17 wild-type (+/+) mice show normal morphology of the myelinated axons in cross-section (black arrows). **F–H**: Electron micrographs of the cerebellar white matter from P17 *Cnp-Cre;Nfasc*$^{Flox}$ mutants show severe axonal pathology and degeneration (F, black arrows). A myelinated axon displays vacuolated and deformed axonal cytoskeleton (G, black arrows). A section through a Purkinje axonal swelling (H) shows accumulation of mitochondria (m) and smooth endoplasmic reticulum (SER) caused by the disorganized paranodal axonal cytoskeleton. Scale bars = 0.2 μm in A, B; 0.1 μm in C,D; 1 μm in E–H.

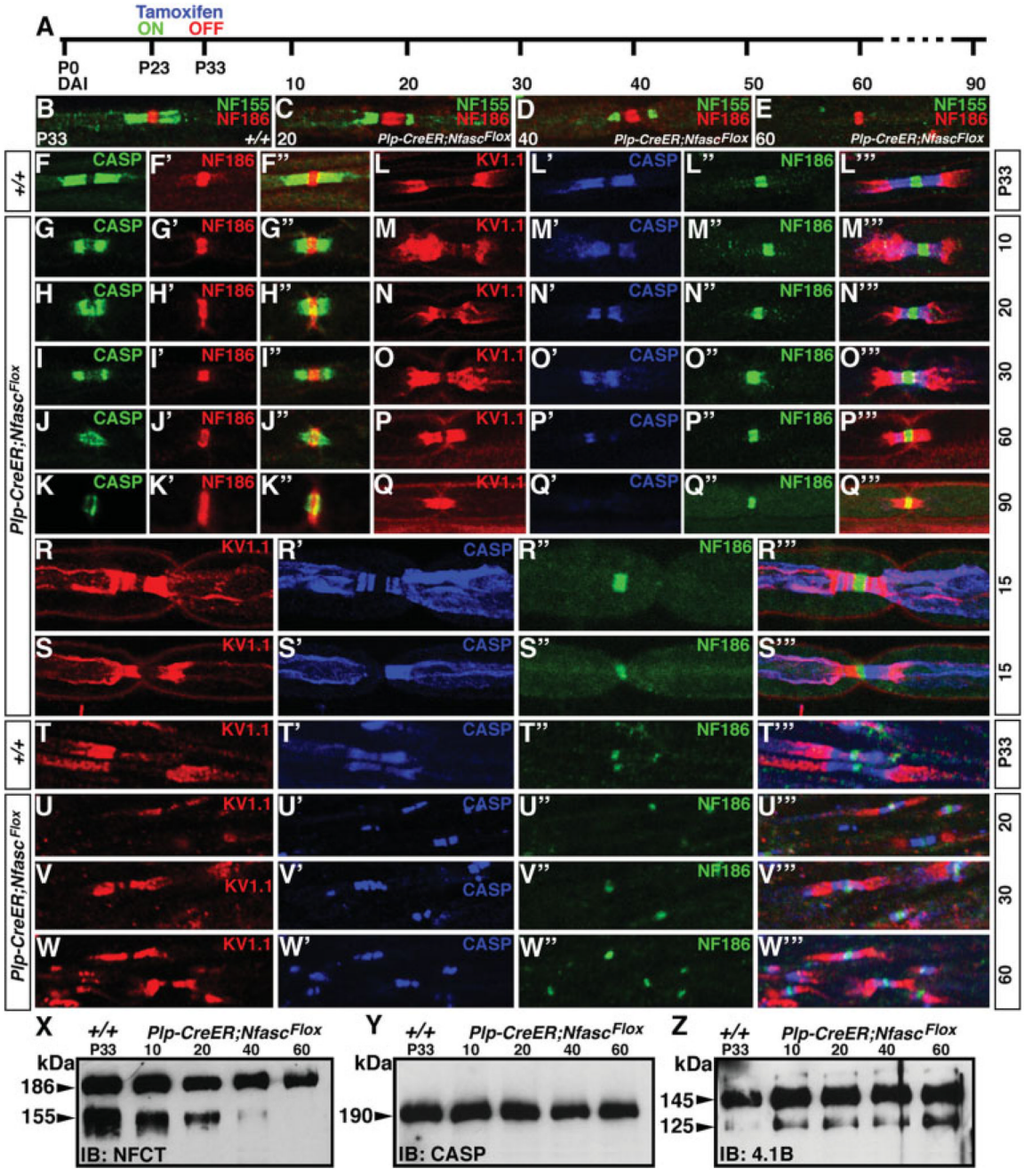


**Fig. 5.**

Maintenance of axonal domains requires intact paranodal axoglial junctions. **A**: Experimental strategy to create myelinating gliaspecific *Nfasc*$^{NF155}$ null adult mutants. Tamoxifen was injected into mice of desired genotypes from P23 to P33, and mice were analyzed at various time points by immunostaining and immunoblotting. **B–E**: Sciatic nerves from wild-type P33 (B, +/+) and tamoxifen-injected P33 *Plp-CreER;Nfasc*$^{Flox}$ mice after 20 (C), 40 (D), and 60 (E) days of injection immunostained with Nfasc$^{NF155}$ (green) and Nfasc$^{NF186}$ (red). The levels of Nfasc$^{NF155}$ at paranodes begin to decrease, and it cannot be detected at 60 days after injection. Nfasc$^{NF186}$ levels are not affected. **F–K″**: Sciatic nerves from P33 wild-type (F–F ″, +/+) and tamoxifen-injected *P33 Plp-CreER;Nfasc*$^{Flox}$ mice after 10 (G– G″), 20 (H–H″),

30 (I–I″), 60 (J–J″), and 90 (K–K″) days of injection immunostained with Caspr (F–K, green) and Nfasc$^{NF186}$ (F′–K′, red). The levels of Caspr at the paranodes begin to fall gradually and could barely be detected at 90 days after injection. At 90 days, the remaining Caspr protein is occasionally seen overlapping with the nodal Nfasc$^{NF186}$ (see merged image in K′). **L–Q‴**: Sciatic nerves from P33 wild-type (L–L‴, +/+) and tamoxifen-injected *P33 Plp-CreER;Nfasc$^{Flox}$* mice after 10 (M–M‴), 20 (N–N‴), 30 (O–O‴), 60 (P–P‴), and 90 (Q–Q‴) days of injection immunostained with juxtaparanodal $K^+$ channel (L–Q, red), paranodal Caspr (L′–Q′, blue), and nodal Nfasc$^{NF186}$ (L″–Q″, green). As Nfasc$^{NF155}$ levels begin to decrease (C–E), Caspr localization at the paranodes also decreases, and concomitantly $K_v$1.1 starts to move toward the node as the paranodal region is getting lost. By 90 days, all of the Caspr is absent at the paranodes, and the domain organization is lost. **R–S‴**: Sciatic nerves from tamoxifen-injected P33 *Plp-CreER;Nfasc$^{Flox}$* mice after 15 of injection immunostained with juxtaparanodal $K^+$ channel (R,S, red), paranodal Caspr (R′–S′, blue), and nodal Nfasc$^{NF186}$ (R″–S″, green) and in merged images (R‴, S‴). These fibers reveal midstages of overlap between juxtaparanodal and paranodal components as axoglial junctions are being compromised. **T–W‴**: Spinal cord sections from P33 wild-type (T–T‴, +/+) and tamoxifen-injected P33 *Plp-CreER;Nfasc$^{Flox}$* mice after 20 (U–U‴), 30 (V–V‴) and 60 (W–W‴) days of injection immunostained with juxtaparanodal $K^+$ channel (T–W, red), paranodal Caspr (T″–W′, blue), and nodal Nfasc$^{NF186}$ (T″–W″, green) and in merged images (T‴–W‴). Note that, even in the presence of remaining Caspr at the paranodes, $K_v$1.1 has already moved next to the nodal region (W‴), indicating that intact axoglial junctions are required to maintain axonal domains. **X–Z**: Immunoblots of spinal cord lysates showing the time course of changes in the levels of Nfasc$^{NF155}$ in *Plp-CreER;Nfasc$^{Flox}$* mice after 10, 20, 40, and 60 days of injection. Note that Nfasc$^{NF155}$ levels begin to fall within 10 days and that by 40 days most of the Nfasc$^{NF155}$ protein is lost (X). On the other hand, protein levels of Caspr (Y) and 4.1B (Z) are not affected by loss of Nfasc$^{NF155}$.

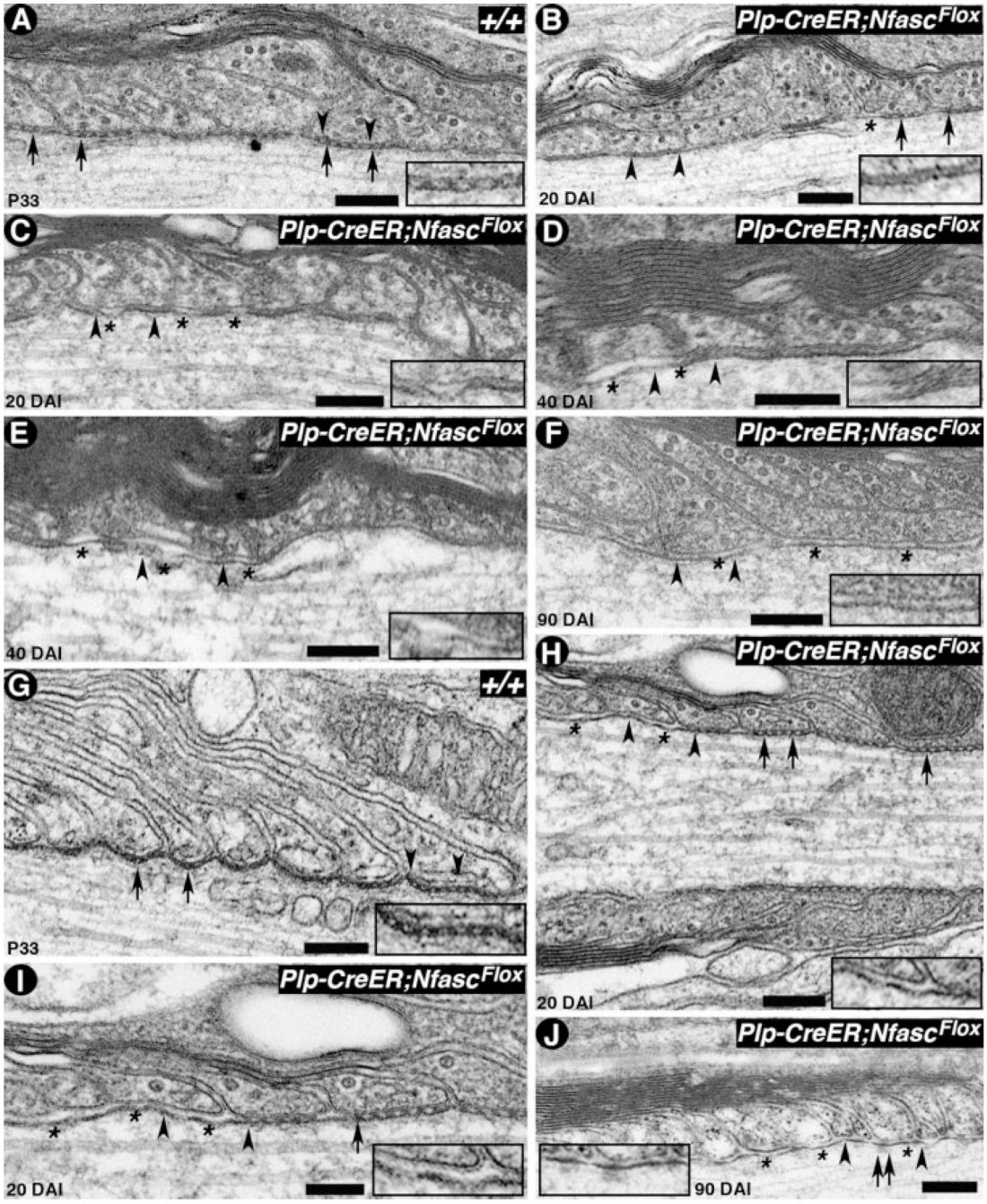


**Fig. 6.**

Axoglial junctions disorganize gradually in *Nfasc*$^{NF155AD}$ adult mutants. **A**: Electron micrograph of a longitudinal section through the paranodal region of a spinal cord fiber from P33 wild-type (+/+) mouse shows paranodal loops tightly apposed to and indenting the axon, forming transverse bands (arrows). The region between the black arrowheads is shown at a higher magnification in the inset. **B–F**: Electron micrographs of longitudinal sections through the paranodal regions of spinal cord nerve fibers from tamoxifen-injected P33 *Plp-CreER;Nfasc*$^{Flox}$ mutants after 20 (B,C), 40 (D,E), and 90 (F) days. At 20 days, transverse band morphology on the right side is still intact (B, black arrows), but on the left side septa have become abnormal and diffuse (B, black arrowheads). Other fibers show diffuse transverse

bands and axolemma detaching from the myelin membrane (C, black arrows, inset). At 40 days, transverse bands remain as unpatterned electron densities (D,E, black arrowheads, insets) and are essentially absent by 90 days (F, black arrowheads, inset). Axolemmal detachments from the myelin membrane are also observed during disorganization of the axoglial junctions (C–F, asterisks). **G**: Electron micrograph of a longitudinal section through the paranodal region of a sciatic nerve fiber from P33 wild-type (+/+) mouse shows paranodal loops forming transverse bands (black arrows). The region between black arrowheads is shown at a higher magnification in the inset. **H–J**: Electron micrographs of longitudinal sections through the paranodal regions of sciatic nerve fibers from tamoxifen-injected *Cnp-Cre;Nfasc*$^{Flox}$ mutants after 20 (H,I) and 90 (J) days. At 20 days, transverse band morphology on the right side is still intact (H, black arrows), but on the left side the transverse bands have already disappeared (H, black arrowheads, inset). At a higher magnification (I), absence of transverse bands (asterisks), diffuse transverse bands, and intact transverse bands are all observed in this fiber. At 90 days, the transverse bands are essentially absent (J, black arrowheads, inset, asterisks). Note that some electron densities on the axolemmal side are still present, which may represent the remaining axonal cytoskeletal complexes at the disorganized paranodes (J, black arrows). Scale bars = 0.2 μm.

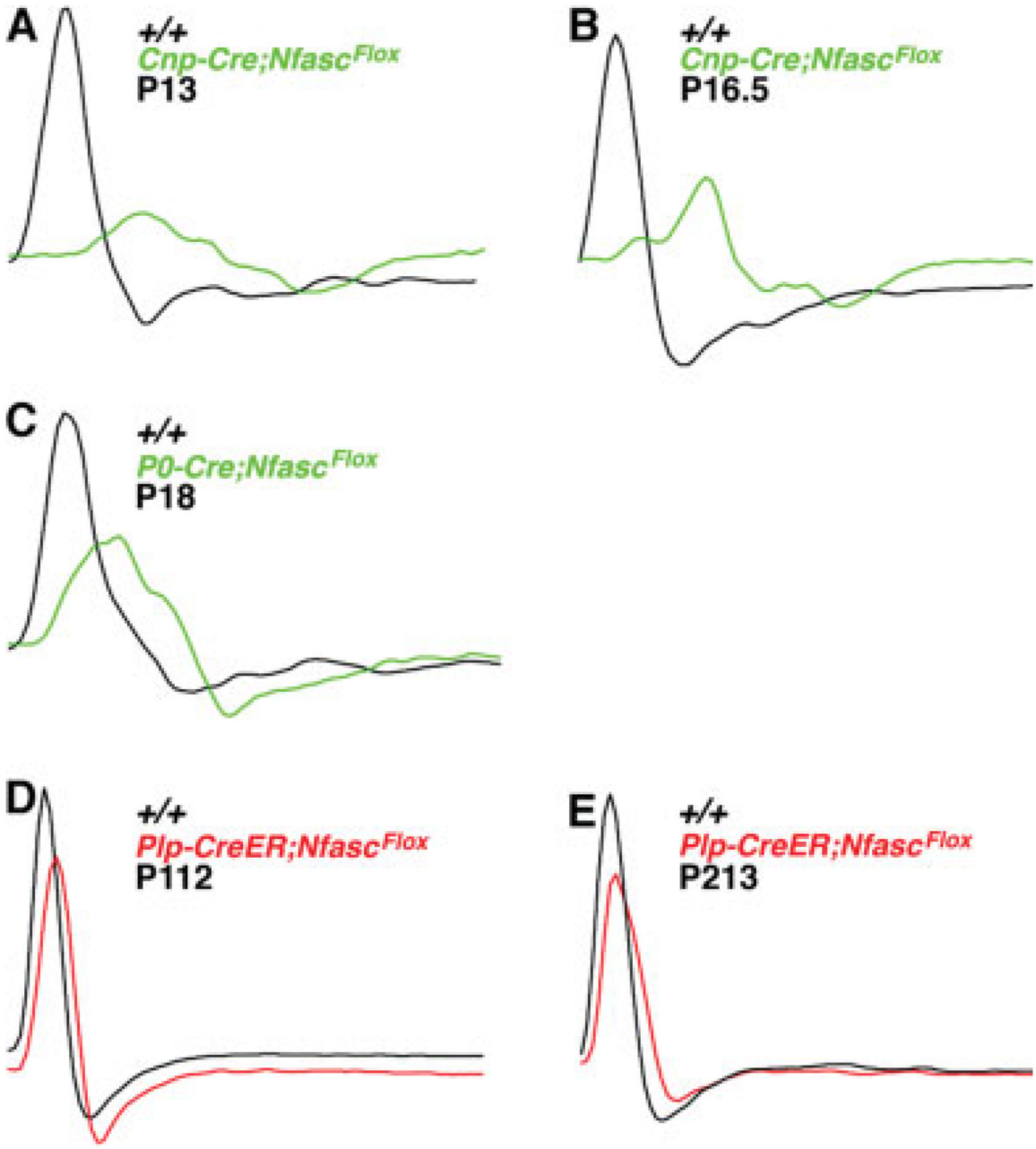


**Fig. 7.**

Peripheral nerve conduction velocities are severely disrupted in *Nfasc*$^{NF155}$ mutants. **A,B**: Representative electrophysiological profiles showing A-component CAPs from P13 wild-type (A, +/+, black) and *Cnp-Cre;Nfasc*$^{Flox}$ (A, green) and P16.5 wild-type (B, +/+, black) and *Cnp-Cre;Nfasc*$^{Flox}$ (B, green) mice show severe conduction delay, decrease in amplitude, and increase in the duration of the action potentials. **C**: Representative electrophysiological profiles A-component CAPs from P18 wild-type (+/+, black) and *P0-Cre;N-fasc*$^{Flox}$ (green) mice show severe conduction delay, decrease in amplitude, and increase in the duration of the action potentials. Thus Cnp- and P0-Cre-mediated deletion of Nfasc$^{NF155}$ independently produce similar electrophysiological deficits, eliminating any major contributions from the genetic

backgrounds of these animals. **D,E**: Representative electrophysiological profiles A-component of CAP from P112 wild-type (E, +/+, black) and tamoxifen-injected *Plp-CreER;Nfasc*$^{Flox/Flox}$ (E, red) and P213 wild-type and tamoxifen-injected *Plp-CreER;Nfasc*$^{Flox/Flox}$ (F, red) mice show a modest delay in conduction and a minimal decrease in amplitude.

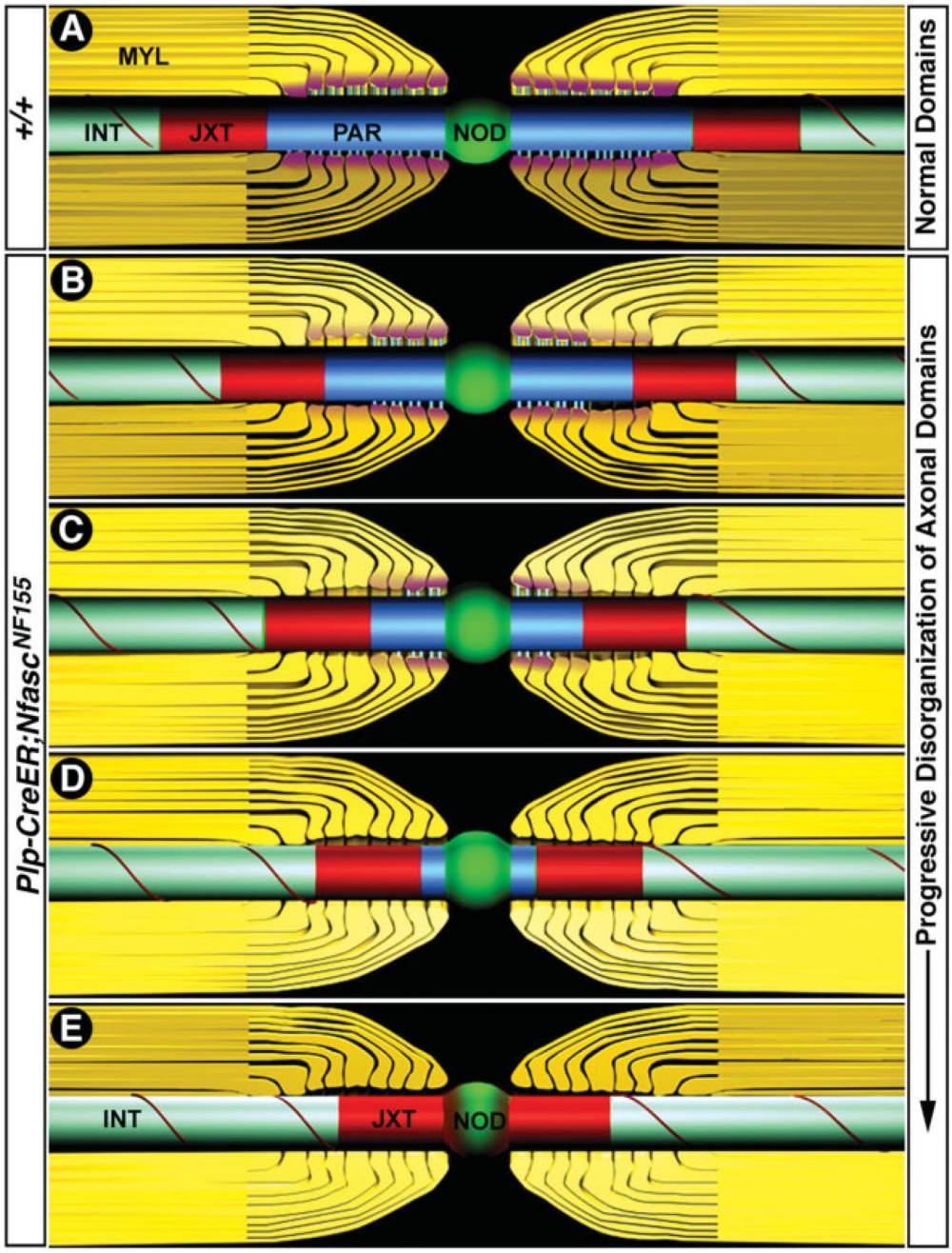


**Fig. 8.**

Schematic illustrations of the loss of axoglial junctions and failure to maintain axonal domains in the peripheral myelinated axons. **A**: Schematic illustration (not to scale) of the axonal domains in wild-type adult myelinated fibers showing node of Ranvier (green), paranodes (blue), and juxtaparanodes (red) and internode (aqua). The internodal region contains compact myelin, and the paranodal region contains loops of noncompact myelin. Molecular interactions between glial $Nfasc^{NF155}$ (pink) and axonal Caspr/contactin (blue) create ladder-like junctions at the paranodal axon–glia interface. The nodal region where $Na^+$ channels are clustered (green) is well separated from the $K^+$ channels at the juxtaparanodal region by the paranodes. **B–E**: Various stages of domain disorganization after tamoxifen-induced *Nfasc*$^{NF155}$ disruption. The

levels of paranodal $Nfasc^{NF155}$ begin to decrease (B, pink), and axoglial junction disorganization starts from the juxtaparanodal region, and $K^+$ channels begin to move into the paranodal region, which begins to get smaller. Axoglial junctions near the nodal region are still intact. $Nfasc^{NF155}$ levels continue to decrease at the paranodes, and more axoglial junctions have been lost, and paranodal region has become smaller (C). $K^+$ channels continue to move toward the node. $Nfasc^{NF155}$ is undetectable at the paranodes (D), and close to 75% of the paranode has been lost. $K^+$ channels continue to move toward the node. Paranodes have disappeared, and $K^+$ channels have reached the nodal region and almost overlap with the nodal $Na^+$ channels. At all stages, the nodal Na1 channels remain clustered and do not seem to diffuse into the paranodal area or the axons. (Note that the illustrations are not to scale and reflect approximate changes in the domain disorganization of the peripheral myelinated axons).

**TABLE I**

Quantitative Analysis of Loss of Paranodal Region and Disorganization of Axonal Domains in Sciatic Nerves of *Nfasc*$^{NF155AD}$ Mutants*

| Genotype | Days after injection[a] | Postnatal age[b] | Paranodes analyzed[c] | Number and Percent of Paranodes[d] Paranodal Length[e] | | | |
|---|---|---|---|---|---|---|---|
| | | | | 100% | 50% | 25% | >10% |
| +/+ | 10 | P43 | 200 | 194 (97) | 6 (3) | 0 | 0 |
| +/+ | 20 | P53 | 190 | 186 (98) | 4 (2) | 0 | 0 |
| +/+ | 90 | P123 | 210 | 206 (98) | 4 (2) | 0 | 0 |
| *Plp-CreER;Nfasc*$^{Flox/Flox}$ | 10 | P43 | 220 | 154 (70) | 37 (18) | 18 (8) | 9 (4) |
| *Plp-CreER;Nfasc*$^{Flox/Flox}$ | 20 | P53 | 200 | 90 (45) | 60 (30) | 30 (15) | 20 (10) |
| *Plp-CreER;Nfasc*$^{Flox/Flox}$ | 90 | P123 | 210 | 10 (5) | 31 (15) | 95 (45) | 74 (35) |
| *Plp-CreER;Nfasc*$^{Flox/Flox}$ | 180 | P213 | 200 | 6 (3) | 10 (5) | 10 (5) | 174 (87) |

[a] Animals were injected with tamoxifen at P23 for 10 days. Injected animals were analyzed by immunofluorescence at various time points.

[b] Postnatal age at the time of tissue analysis after tamoxifen injection (see Fig. 5, Fig 6 and Fig 7 for details).

[c] Total number of paranodes analyzed based on the immunoreactivity against paranodal Caspr and nodal NF186.

[d] The average length of the paranodal region was based on Caspr immunoreactivity compared to average wild-type length (generally 4–5 μm using calibrated preetched micrometer-grid slides from Zeiss). If the variation between paranodes was less than 10%, they were grouped with the next lower percentage. Variations in length that exceeded 11% were grouped in the next higher percentage. Paranodes that appeared too stretched from mechanical teasing during preparation were not included in the estimates.

[e] Paranodal lengths were estimated as 100%, if they measured 4–5 μm, 50% for 2–2.5 μm, 25% for 1–1.25 μm, and <10% at 0.5 μm and lower.

## TABLE II

Electrophysiological Measurements of Tibial/Plantar Nerve Conduction Velocities

| *Nfasc* allele | Genotype | CV (m/sec mean ± SEM) | Postnatal age (mean days) | n |
|---|---|---|---|---|
| WT | +/+ | 16.9 ± 0.09 | 13 | 4 |
| $Nfasc^{NF155}$ | *Cnp-Cre*/+; $Nfasc^{Flox/Flox}$ | 9.5 ± 0.97 | 13 | 4 |
| WT | +/+ | 21.75 ± 4.12 | 21 | 4 |
| $Nfasc^{NF155}$ | *P0-Cre;* $Nfasc^{Flox/Flox}$ | 12.83 ± 2.86 | 21 | 4 |
| WT | +/+ | 33.50 ± 4.30 | 86[a] | 2 |
| $Nfasc^{NF155AD}$ | *Plp-CreER;* $Nfasc^{Flox/Flox}$ | 25.60 ± 5.60 | 86[a] | 2 |

[a] Animals were injected at P23 for 10 days and allowed to age to specified time points for electrophysiological measurements.